Air-sea gas transfer: Its dependence on wind stress, small-scale roughness, and surface films

Nelson M. Frew,[1] Erik J. Bock,[2,3] Uwe Schimpf,[2] Tetsu Hara,[4] Horst Haußecker,[2,5] James B. Edson,[1] Wade R. McGillis,[1,6] Robert K. Nelson,[1] Sean P. McKenna,[1] B. Mete Uz,[4,7] and B. Jähne[2]

Received 19 September 2003; revised 14 July 2004; accepted 16 July 2004; published 21 August 2004.

[1] The influence of wind stress, small-scale waves, and surface films on air-sea gas exchange at low to moderate wind speeds (<10 m s^{-1}) is examined. Coincident observations of wind stress, heat transfer velocity, surface wave slope, and surface film enrichments were made in coastal and offshore waters south of Cape Cod, New England, in July 1997 as part of the NSF-CoOP Coastal Air-Sea Chemical Fluxes study. Gas transfer velocities have been extrapolated from aqueous heat transfer velocities derived from infrared imagery and direct covariance and bulk heat flux estimates. Gas transfer velocity is found to follow a quadratic relationship with wind speed, which accounts for ~75–77% of the variance but which overpredicts transfer velocity in the presence of surface films. The dependence on wind stress as represented by the friction velocity is also nonlinear, reflecting a wave field-dependent transition between limiting transport regimes. In contrast, the dependence on mean square slope computed for the wave number range of 40–800 rad m^{-1} is found to be linear and in agreement with results from previous laboratory wind wave studies. The slope spectrum of the small-scale waves and the gas transfer velocity are attenuated in the presence of surface films. Observations over large-scale gradients of biological productivity and dissolved organic matter show that the reduction in slope and transfer velocity are more clearly correlated with surface film enrichments than with bulk organic matter concentrations. The mean square slope parameterization explains ~89–95% of the observed variance in the data and does not overpredict transfer velocities where films are present. While the specific relationships between gas transfer velocity and wind speed or mean square slope vary slightly with the choice of Schmidt number exponent used to scale the heat transfer velocities to gas transfer velocities, the correlation of heat or gas transfer velocity with mean square slope is consistently better than with wind speed. *INDEX TERMS:* 0312 Atmospheric Composition and Structure: Air/sea constituent fluxes (3339, 4504); 4504 Oceanography: Physical: Air/sea interactions (0312); 4506 Oceanography: Physical: Capillary waves; 4820 Oceanography: Biological and Chemical: Gases; 4806 Oceanography: Biological and Chemical: Carbon cycling; *KEYWORDS:* air-sea gas transfer, small-scale waves, surface films

Citation: Frew, N. M., et al. (2004), Air-sea gas transfer: Its dependence on wind stress, small-scale roughness, and surface films, *J. Geophys. Res.*, *109*, C08S17, doi:10.1029/2003JC002131.

1. Introduction

[2] Regional and global oceanic gas flux estimates based on air-sea exchange models have assumed new importance because of the current interest in the role of the oceans as a sink or source for anthropogenic CO_2 and other climatically important gases. However, the kinetics and underlying mechanisms of air-sea gas transfer are not well understood. The forcing of surface waves and subsurface turbulence by wind is clearly a key factor in the enhancement of gas transfer. Thus numerous empirical relationships between gas transfer velocity (k) and wind speed at 10 m height (U_{10}), have been put forward [*Liss and Merlivat*, 1986; *Wanninkhof*, 1992; *Tans et al.*, 1990; *Erikson*, 1993; *Wanninkhof and McGillis*, 1999; *Nightingale et al.*, 2000a; *McGillis et al.*, 2001a, 2001b]. Each of these relationships

[1]Woods Hole Oceanographic Institution, Woods Hole, Massachusetts, USA.
[2]Interdisciplinary Center for Scientific Computing, University of Heidelberg, Heidelberg, Germany.
[3]Deceased June 2001.
[4]Graduate School of Oceanography, University of Rhode Island, Narragansett, Rhode Island, USA.
[5]Now at Intel Corporation, Santa Clara, California, USA.
[6]Now at Lamont-Doherty Earth Observatory, Columbia University, Palisades, New York, USA.
[7]Now at Earth System Science Interdisciplinary Center, University of Maryland, College Park, Maryland, USA.

0148-0227/04/2003JC002131$09.00

generally has been derived from a relatively limited set of observations. Considering the entire range of valid field measurements of gas transfer velocity that have been reported over the past few decades, however, these individual relationships do not explain a significant portion of the observed variance [see, e.g., *Donelan and Wanninkhof*, 2002]. Some of this uncertainty may be ascribed to the difficulty of making in situ gas flux measurements over a wide range of wind speeds, particularly on timescales commensurate with variability in the wind speed. However, it also appears that k does not depend solely on wind speed [*Jähne et al.*, 1979, 1987a; *Frew et al.*, 1995; *Frew*, 1997; *Hara et al.*, 1995; *Bock et al.*, 1999; *Wanninkhof and McGillis*, 1999; *Nightingale et al.*, 2000a]. Both laboratory and field data exhibit considerable scatter when correlated with either U_{10} or the air-side friction velocity u_{*a}, where $\tau = \rho_a u_{*}^2 a$ is the wind stress and ρ_a is the air density. Wave fetch [*Wanninkhof*, 1992], boundary layer instability [*Erickson*, 1993], and the presence of surface–active organic matter [*Frew et al.*, 1990, 1995; *Bock et al.*, 1995; *Frew*, 1997; *Frew and Nelson*, 1999] have all been cited as factors that have a strong influence on k. These factors modify both the small-scale wave field (surface roughness) and subsurface turbulence field, and hence modify the transfer velocity. Thus, despite the obvious role of wind in enhancing gas exchange, no unique, tightly constrained relationship between wind speed and transfer velocity is apparent.

[3] Primarily two processes control air-sea gas transfer, namely, exchange due to turbulent and diffusive transport across the ocean surface skin layer and exchange due to bubbles injected by surface breaking waves. As an aside, we note that, in recent literature, turbulent processes leading to enhanced transport across the ocean surface are often loosely (and incorrectly) referred to as 'surface renewal'. In this paper, however, we restrict the use of this term to the formalism of the surface renewal model as originally described by *Higbie* [1935] and later extended by *Danckwerts* [1951], in which random replacement of water parcels at the surface is both complete and instantaneous. This is to be clearly distinguished from turbulent perturbations of the aqueous boundary layers that result in enhanced gas transport but do not necessarily involve complete and instantaneous renewal of the water surface. Although occurrence of enhanced turbulence and surface renewal events at the water surface can be easily visualized using infrared techniques, the underlying physical mechanisms are not fully understood. It has been suggested that intermittent large breaking events may be responsible for enhanced transport because recent observations show elevated turbulence dissipation rates in the near-surface water layer when large breaking events occur [*Agrawal et al.*, 1992; *Drennan et al.*, 1996; *Terray et al.*, 1996]. However, more recent studies indicate that two small-scale physical processes mainly enhance gas transport: microscale breaking of short wind waves (wavelength 0.1–0.5 m) and small-scale (Langmuir-type) eddies generated by wave-current interactions.

[4] *Csanady* [1990] has proposed that the effective process is generation of surface convergence/divergence during microscale breaking of short gravity waves. Experimentally, *Jessup et al.* [1997] have identified regions of enhanced turbulence due to microscale breaking of short wind waves in laboratory tanks and in situ using an infrared imaging technique. *Zappa et al.* [2001] have further demonstrated that the spatial coverage of microscale breaking strongly correlates with the gas transfer velocity. Measurements of 2-D velocity fields beneath microscale breaking waves using particle-imaging velocimetry have demonstrated that small-scale vortices are generated just behind microscale breaking crests [*Siddiqui et al.*, 2001]. *Siddiqui et al.* [2004] have shown that this enhanced near-surface vorticity can account for most of the enhancement of gas exchange observed by *Zappa* [1999]. These studies clearly demonstrate that a significant fraction of gas exchange is associated with microscale breaking, particularly at moderate to high winds. In addition, turbulence very close to the air-sea interface may be enhanced by wind-wave interactions (Langmuir-type instability) in the presence of gravity-capillary and short gravity waves. This has been clearly demonstrated both in laboratories [*Melville et al.*, 1998; *Veron and Melville*, 2001] and in the field [*Gemmrich and Hasse*, 1992].

[5] It is noteworthy that both processes discussed above require the presence of small-scale wind waves in addition to wind forcing. Therefore it is not surprising that recent work has focused on the role of small-scale surface waves in controlling the kinetics of gas exchange. Several laboratory studies have demonstrated a strong correlation between the gas transfer velocity for sparingly soluble gases and the mean square slope, $\langle S^2 \rangle$. *Jähne et al.* [1984] were the first to suggest such a connection. Their laboratory experiments showed a clear correlation between gas transfer velocity and total mean square surface slope. Their comparison of data from wind-wave tanks of different scales suggested that waves of all wavelengths contribute to enhanced turbulence and gas exchange. More recent gas transfer experiments in laboratory wave tanks [*Hara et al.*, 1995; *Frew*, 1997; *Bock et al.*, 1999], in which synthetic surfactants were used to modulate small-scale wind-driven waves, also demonstrated a significant relationship between k and total mean square surface slope. This relationship held for a range of surfactant concentrations comparable to those found in coastal and open ocean environments. However, small-scale waves (wave number $\kappa > 25$ rad m^{-1}) appeared to play a dominant role since mean square surface slope was increasingly well correlated with k for wave numbers above 25 rad m^{-1}. The same studies showed a poor correlation between k and U_{10} or friction velocity u_*, except in the case of very clean, surfactant-free water. This strongly suggested the use of mean square slope calculated over an appropriate wave number range, rather than U_{10} or u_*, as the parameter of choice to represent gas transfer velocity [*Bock et al.*, 1999] under wind-generated forcing. Recently, *Zappa et al.* [2002] provided experimental evidence that microscale breaking is one of the key underlying processes linking mean square slope and gas transfer. They showed that mean square slope is strongly enhanced (up to 60%) by roughness features associated with waves undergoing microscale breaking in a laboratory facility.

[6] Observations of gas transfer made in laboratory wind-wave facilities provide valuable mechanistic insights but can't be extrapolated easily to oceanic conditions. Relatively few field data have been available to compare with the laboratory studies. Recently developed tools have made more detailed field investigations possible. Techniques for measurement of heat and mass fluxes, particularly the direct

covariance, boundary layer concentration profile and infrared imaging methods [*Edson and Fairall*, 1998; *Fairall et al.*, 2000; *McGillis et al.*, 2001a, 2001b; *Jähne and Haußecker*, 1998; *Haußecker et al.*, 2002; *Schimpf et al.*, 2002; *Garbe et al.*, 2002] have greatly improved during the last few years. Flux measurements can now be made on timescales that more closely match variability in environmental forcing parameters, i.e., seconds to hours as compared to days or weeks for previous tracer methods [*Peng et al.*, 1979; *Upstill-Goddard et al.*, 1991; *Wanninkhof et al.*, 1993]. Also, robust instruments for the in situ characterization of the small-scale wave slope spectrum have been developed [*Bock and Hara*, 1995]. In this paper we describe results of efforts to use these new tools to examine the relationship between in situ gas exchange rates and critical forcing parameters.

2. CoOP Coastal Gas Exchange Experiments

[7] As part of the NSF-sponsored Coastal Ocean Processes (CoOP) program 'Coastal Air-Sea Chemical Fluxes,' studies of coastal air-sea gas exchange were conducted from the R/V New Horizon off California in April/May 1995 and from the R/V *Oceanus* in coastal and offshore waters south of Cape Cod in June/July 1997. The objective of these studies was to understand the effects of atmospheric, oceanic, and interfacial processes on air-sea gas exchange. Jointly, groups from the Woods Hole Oceanographic Institution, the University of Rhode Island and the University of Heidelberg deployed a new suite of in situ instruments to measure gas transfer velocity, wind speed, wind stress, surface wave slope, and surface microlayer chemical enrichment on the short timescales commensurate with natural forcing variability.

[8] Measurements were made with ship-based instrumentation and with a newly developed remotely operated research catamaran (LADAS). The ship-based systems included a high-resolution infrared imager used to measure the sea surface temperature distribution and the skin-bulk temperature difference, and a meteorological package used to estimate momentum, heat and moisture fluxes. The catamaran carried a scanning laser slope gauge to quantify the surface wave characteristics and an additional meteorological package to quantify the near-surface atmospheric turbulence. A fluorometry package measured surface microlayer enrichments of colored dissolved organic matter (CDOM) as a limited proxy for surface films.

[9] These field experiments yielded the first coincident measurements of atmospheric forcing, small-scale surface roughness, surface chemical enrichment, and gas transfer rates, allowing several aspects of gas exchange mechanisms to be studied. Initial gas exchange results from the CoOP experiments have been published by *Haußecker* [1996], *Jähne and Haußecker* [1998], and *Schimpf et al.* [2002]. Here we present a more complete analysis of gas transfer measurements made with high spatiotemporal resolution during the 1997 experiment (hereafter referred to as CoOP97) along with a description and integration of the physical and chemical measurements.

[10] The CoOP97 study area and station locations are shown in Figure 1, along with the climatological CZCS chlorophyll data for the month of July (1978–1986). The stations covered a significant gradient of biological productivity and dissolved organic matter concentrations as indicated in Table 1. Near-surface chlorophyll values ranged from 0.05 to 2 mg m^{-3} and DOC concentrations ranged from 75 to 110 μg L^{-1}. Surface-active organic matter (SAOM) concentrations varied by an order of magnitude (0.13–1.2 mg L^{-1}) and CDOM concentrations varied by a factor of 23 (0.06–1.4 μg L^{-1}).

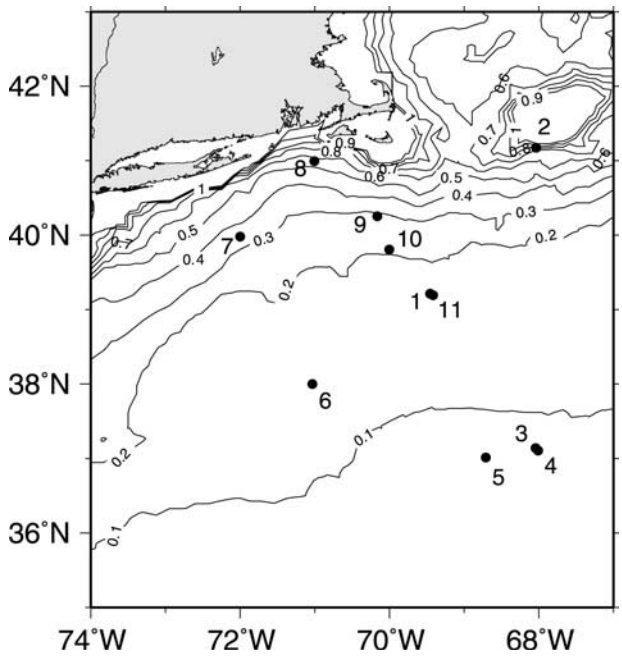

Figure 1. Chart of study area and stations south of Cape Cod, Massachusetts, occupied during the July 1997 CoOP Coastal Air-Sea Chemical Fluxes Experiment. The July (1978–1986) climatological CZCS chlorophyll values (mg m^{-3}) are shown contoured at 0.1 mg m^{-3} intervals. Station coordinates and ancillary physical and chemical information are given in Table 1.

3. Experimental Methodology

3.1. Thermal Imagery

[11] Thermal imaging techniques allow the use of heat as a proxy tracer for gases to study the molecular transport process across the air-water interface. The analysis of highly temporally (60 Hz) and spatially (3 mm) resolved infrared image sequences gives a direct insight into the mechanisms of exchange processes across the aqueous thermal boundary layer and enables fast measurements of the local heat transfer velocity [*Schimpf et al.*, 2004]. The latent and sensible heat flux at the ocean surface, as well as long wave emission of radiation, force the surface temperature to deviate from the bulk temperature. Since the net heat flux is mostly directed upward from the ocean surface, the resulting temperature difference across the thermal boundary layer, known as the 'cool skin' of the ocean, is of the order of a few tenths of a degree. The temperature fluctuations occurring at the sea surface, which are associated with the transport processes in the aqueous thermal boundary layer, can be detected using state-of-the-art digital infrared cameras. Figure 2c shows the instrument during the field campaign, mounted on a boom at the bow of the R/V *Oceanus*. The main part of the instrument (see schematic

Table 1. Chemical and Physical Parameters for Stations Occupied During the July 1997 CoOP Coastal Gas Exchange Experiment (see Figure 1)[a]

Station	1	2	3	4	5	6	7	8	9	10	11
Yearday	188	189	190	191	192	193	194	195	196	197	198
Latitude, N	39.21	41.17	37.10	37.14	37.01	37.99	39.98	41.00	40.25	39.81	39.19
Longitude, W	69.45	68.04	68.01	68.04	68.71	71.04	72.00	71.01	70.16	70.02	69.41
SST, °C	22.7	14.3	27.5	27.8	25.6	23.9	22.1	20.17	21.5	24.3	25.1
Salinity, psu	35.8	33.6	37.9	38.0	38.0	36.2	32.0	33.1	33.4	36.1	36.3
DOC, μM	87	82	76	N.D.	74	88	108	90	97	84	88
Chlorophyll, mg m^{-3}	0.12	2.1	0.07	N.D.	0.08	0.2	0.3	0.5	0.47	0.15	0.07
SAOM, mg L^{-1}	0.68	1	0.13	N.D.	<0.05	0.25	1.2	0.91	0.83	0.33	0.32
CDOM at 10 cm, ppb	0.19	0.73	0.06	N.D.	0.06	0.25	1.4	1.1	1.0	0.27	0.20
Avg ΔCDOM, ppb	0.16	0.23	0.03	N.D.	0.22	0.02	0.04	0.02	N.D.	0.03	0
Avg U_{10}, m s^{-1}	2.5	5.2	2.1	7.6	3.4	4.1	4.3	5.8	6.2	6.0	8.5
Avg. S(κ) (κ = 100 rad m^{-1})	3.30 E−09	3.82 E−08	1.82 E−07	N.D.	2.55 E−07	2.96 E−07	1.98 E−07	2.33 E−07	3.03 E−07	N.D.	4.27 E−07
Avg. S(κ) (κ = 200 rad m^{-1})	1.45 E−09	2.12 E−09	2.45 E−08	N.D.	7.73 E−08	5.33 E−08	3.03 E−08	4.27 E−08	5.99 E−08	N.D.	1.51 E−07
Avg. S(κ) (κ = 400 rad m^{-1})	1.99 E−10	5.02 E−10	7.29 E−09	N.D.	2.82 E−08	1.51 E−08	8.52 E−09	1.10 E−08	1.63 E−08	N.D.	5.00 E−08
Avg. transfer velocity k, cm h^{-1}	0.5	1.3	4.4	17.2	4.5	5.9	3.5	6.2	7.6	9.1	16.2

[a]N.D. = No Data.

sketch, Figure 2a) combined an infrared imager (Raytheon Amber Radiance 1: 256 × 256 pixel focal plane array, sensitive in the wavelength region from 3–5 μm, 60 frames s^{-1}, noise equivalent temperature difference 26 mK [*Schimpf*, 2000]), a blackbody calibration device [*Haußecker*, 1996], and a standard PC with a PCI frame grabber (Bitflow Raptor). The infrared detector was directed at the water surface at an incidence angle of 20° and sequences of eight images each were recorded every 10 s. Figure 2b shows a single infrared image (image size: 60 × 60 cm) acquired during the field campaign. *Haußecker* [1996] presented an approach referred to as the passive controlled flux technique, capable of estimating the temperature difference across the thermal boundary layer under natural heat flux conditions, as occurring at the ocean surface. The details of this approach have been presented previously [*Haußecker*, 1996; *Jähne and Haußecker*, 1998; *Schimpf et al.*, 2002; *Schimpf et al.*, 2004]. Assuming a surface renewal model with depth-independent renewal rate [*Danckwerts*, 1970], the theoretical distribution of the sea surface temperature is calculated. Fitting this function to the observed temperature distribution (Figure 2d) gives an estimate of the temperature difference across the thermal boundary layer ($\Delta T = T_{surface} - T_{bulk}$). *Schimpf et al.* [2004] have presented experimental results showing excellent agreement (within 10%) between ΔT estimated thermographically from the observed temperature distribution and ΔT measured using a second infrared method in which the mean temperature difference was determined by switching between conditions of negative and zero heat flux. The statistical thermographic approach was applied to each image sequence. The ΔT values were averaged over 15 min to match the temporal resolution of the micrometeorological heat flux estimates. Given the net heat flux at the water surface, j_{heat}, from the micrometeorological measurements, the transfer velocity for heat then could be calculated.

3.2. Gas Transfer Velocity

[12] The surface skin-bulk temperature difference across the thermal boundary layer, ΔT, and the net heat flux density at the ocean surface, j_{heat}, are related by the transfer velocity for heat, k_{heat}, according to [*Jähne et al.*, 1989]:

$$k_{heat} = \frac{j_{heat}}{\rho c_p \Delta T}, \tag{1}$$

where ρ is density and c_p is the specific heat of seawater. From heat transfer velocities, k_{heat}, the transfer velocities, k_{gas}, of arbitrary gases can be obtained using Schmidt number scaling:

$$k_{gas} = k_{heat}\left[\frac{Sc}{Pr}\right]^{-n}, \tag{2}$$

where Sc is the Schmidt number, the ratio of the kinematic viscosity to the molecular diffusivity of the gas ($Sc = \nu/D$) and Pr is the Prandtl number, the analogous ratio for heat. Although the difference between the Prandtl number for heat and the Schmidt number for a typical gas is large (e.g., Pr = 7, Sc = 660 for CO_2 in seawater at 20°C), previous measurements [*Jähne et al.*, 1989] have shown that this extrapolation is correct to within about 10% if the uncertainty in D is less than 5% and the Schmidt number exponent n is known with an error of less than ±0.02. However, the Schmidt number dependence is likely to vary as a function of wind stress, wave slope, and near-surface turbulence. The exact form of this dependence is not known. In wind-wave flume experiments in which the wave field was manipulated by varying u_{*w} and surface film concentration, *Jähne et al.* [1984] found evidence that n varies systematically with mean square slope, undergoing a smooth sigmoid-shaped transition between ~0.7 and 0.5 as wave slope increases. More recent data also showing a gradual variation of n with u_{*w} and $\langle S^2 \rangle$ are cited by *Jähne and Haußecker* [1998].

[13] We therefore looked at the sensitivity of the transfer velocity–wind speed and transfer velocity–mean square slope relationships to assumptions about the Schmidt number dependence. In scaling our estimated heat transfer

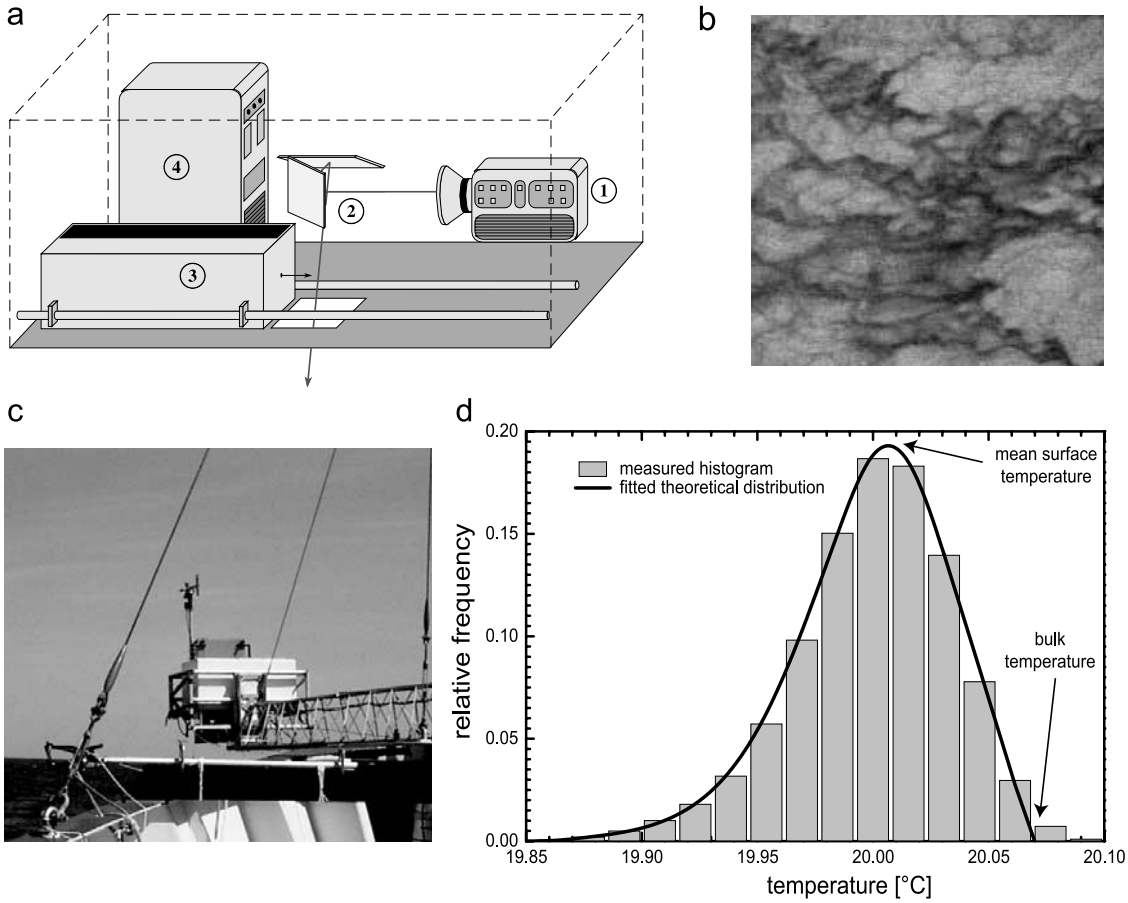

Figure 2. (a) Schematic sketch of the infrared instrument: 1, infrared imager; 2, mirrors; 3, blackbody calibration device; and 4, PC for data acquisition. (b) Infrared image of the ocean surface; image size: 60 × 60 cm. (c) Instrument mounted on a boom at the bow of the R/V *Oceanus*. (d) Observed temperature histogram fitted with the theoretical sea surface temperature distribution based on the surface renewal model.

velocities to gas transfer velocities according to equation (2), we defined three hydrodynamic regimes based on mean square slope thresholds, t_1 and t_2: (regime 1) a smooth water surface, for which $\langle S^2 \rangle_{\kappa=40-800} < t_1$ and $n = 0.67$, (regime 2) a transition state where n is between 0.67 and 0.5 (assumed to be 0.59 ± 0.09), and (regime 3) a free wavy surface, for which $\langle S^2 \rangle_{\kappa=40-800} \geq t_2$ and $n = 0.5$. As a default scenario, we chose $t_1 = t_2 = 2E{-}03$, since this choice of thresholds was partially supported by visual observations of slicked sea surfaces and by high values of ΔCDOM, the excess CDOM concentration at the air-sea interface relative to the subsurface water [*Frew et al.*, 2002]. We also report results for two other scaling scenarios, one in which $t_1 = 2E{-}03$ and $t_2 = 8E{-}03$, and another in which $t_1 = 4E{-}03$ and $t_2 = 2E{-}02$. In the latter scenario, the chosen thresholds correspond roughly to the experimental laboratory results reported by *Jähne and Haußecker* [1998]; in the former scenario, t_1 was chosen as in the default case, but t_2 was chosen arbitrarily to illustrate the effect of an intermediate value of t_2. In cases where mean square slope values were not available, n was assigned on the basis of consideration of wind stress and ΔCDOM levels.

[14] A few caveats apply to our use of the thermographic technique to estimate transfer velocities. We point out that consideration of Schmidt number exponents other than 0.5 to allow for the effects of surface films on the wave field and near-surface turbulence introduces an apparent contradiction of the surface renewal model formalism, which predicts that $n = 0.5$. The estimation of ΔT from the observed surface temperature distributions in the infrared images and therefore also of k_{heat}, is based on the theoretical temperature distribution derived from the surface renewal model. T_{bulk} will be underestimated, for example, in the case of a cool ocean skin, if parcels of the water surface are not occasionally completely replaced. It appears, however, that ΔT can be determined reasonably accurately for film-influenced water surfaces, even as the films begin to modify the turbulence field, as long as some surface renewal events occur. There is considerable evidence in the gas transfer literature to suggest that surface renewal events continue to occur as surface film contamination increases, but over smaller net areas and then less frequently [*Davies*, 1970; *Springer and Pigford*, 1970; *Lee et al.*, 1980; *Asher and Pankow*, 1989, 1991; *Münsterer and Jähne*, 1998]. *Springer and Pigford* [1970], for example, showed that the Danckwerts distribution function for surface age is still approximately valid in the presence of surface films at low film pressures. The surface temperature distributions observed in the infrared images should continue to reflect these renewal events and one can argue that the function

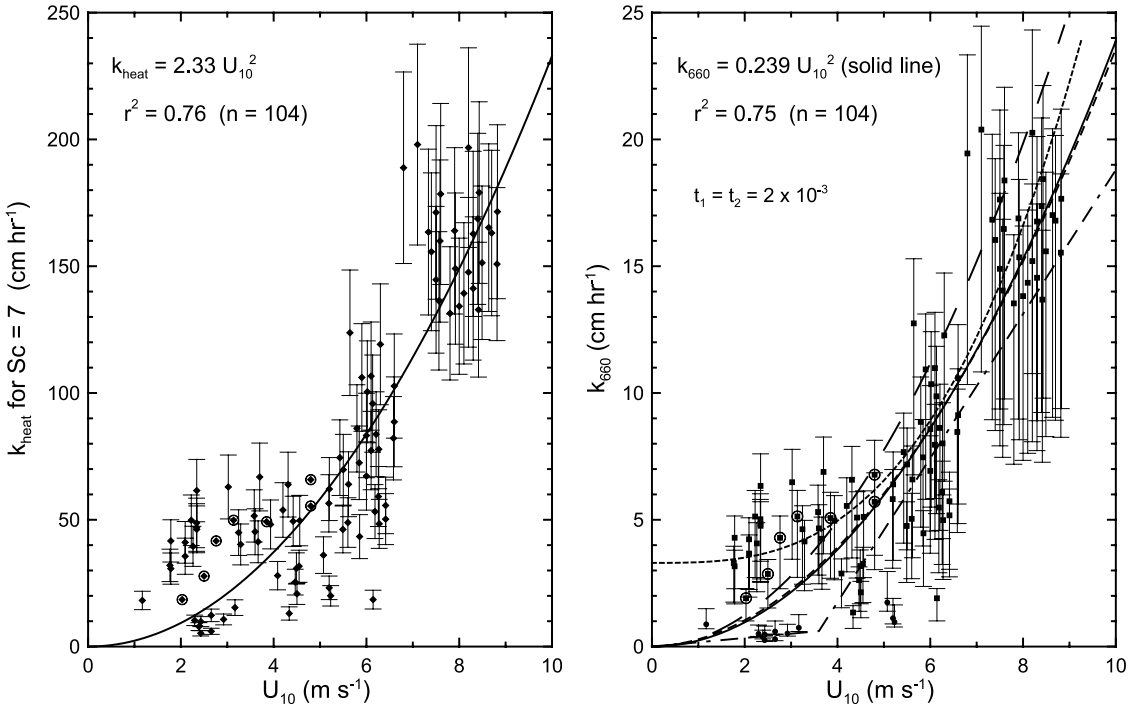

Figure 3. (left) Heat transfer velocity k_{heat} and (right) gas transfer velocity velocity k_{660} versus wind speed U_{10}. Solid diamonds, unscaled k_{heat}; solid circles, k_{660} ($n = 0.67$); and solid squares, k_{660} ($n = 0.5$). Schmidt number exponents used to scale k_{heat} to k_{660} were assigned using mean square slope criterion $t_1 = t_2 = 2E{-}03$ (see text). Circled points represent data collected during light to heavy rain events. Quadratic best fits for 104 data pairs are shown as solid lines ($k_{heat} = 2.33U_{10}^2$, coefficient of determination $r^2 = 0.76$; $k_{660} = 0.239U_{10}^2$, $r^2 = 0.75$). Several idealized transfer velocity-wind speed relationships are included for comparison: *Nightingale et al.* [2000b] (medium dash); *Wanninkhof* [1992] (long dash), *Liss and Merlivat* [1986] (short long dash), and *McGillis et al.* [2001a] (short dash). Error bars represent combined error estimated from uncertainty in j_{heat}, ΔT, and Schmidt number scaling exponent.

used to fit the temperature distribution still leads to a robust estimate of T_{bulk}, even though it is based on the surface renewal formalism. This contention is supported by the recent experimental data of *Schimpf et al.* [2004], which show excellent agreement between the ΔT estimates made using theoretical fits based on surface renewal and the directly measured mean temperature differences. Those data include results from film-influenced surfaces. The fitting process clearly breaks down, however, when the water surface is heavily filmed and surface renewal events are extinguished. *Schimpf et al.* [2004] reported significant underestimates of ΔT using the thermographic technique in cases of low wind and heavily filmed surfaces. Thus, in those cases where heavily slicked and low wind conditions were encountered during CoOP97, a significant systematic bias toward lower ΔT and higher k_{heat} may have been introduced as a result of the methodology; this is discussed further in section 4.1.

[15] Similarly, the scaling of k_{heat} to higher Schmidt numbers (e.g., to k_{gas} at Sc = 660) using n other than 0.5, as described above, is not strictly in conformance with the surface renewal model. However, considering the temporal average, independent of any model (e.g., surface renewal or small eddy), one can define a thermal or mass boundary layer and calculate a mean temperature (or gas) concentration profile for different Schmidt number exponents. The work of *Münsterer and Jähne* [1998] to experimentally measure such boundary layer profiles showed that, for a nearly smooth surface, parts of this 'boundary layer' were being swept into the bulk and that the measured mean concentration profiles were better predicted by a surface renewal model with $n = 0.67$ than by surface renewal with $n = 0.5$, or by the small eddy model with either value of n. Thus it seems reasonable to consider intermediate values of n in scaling k_{heat} to higher Schmidt numbers.

[16] It is also important to note that the CoOP97 observations were made for a range of wind speeds up to 10 m s^{-1}, and that breaking waves and associated bubble plumes were present at the upper wind speeds. While the gas transfer velocities determined by the infrared method generally include the effect of turbulence introduced by the breaking process, they do not incorporate the effects of bubble-mediated gas transfer processes other than bubble-generated turbulence.

3.3. Meteorological Parameters

[17] Direct air-sea flux measurements were made using a turbulent flux measurement system mounted on the forward jack staff of the R/V *Oceanus*. As on any seagoing research vessel, the platform motion complicated the measurement of the vertical wind velocity necessary to compute the covariance and this motion contamination had to be removed before the fluxes could be estimated. The integrated Direct Covariance Flux System (DCFS) is capable of correcting for the velocity of the ship motion [*Edson et al.*, 1998]. The

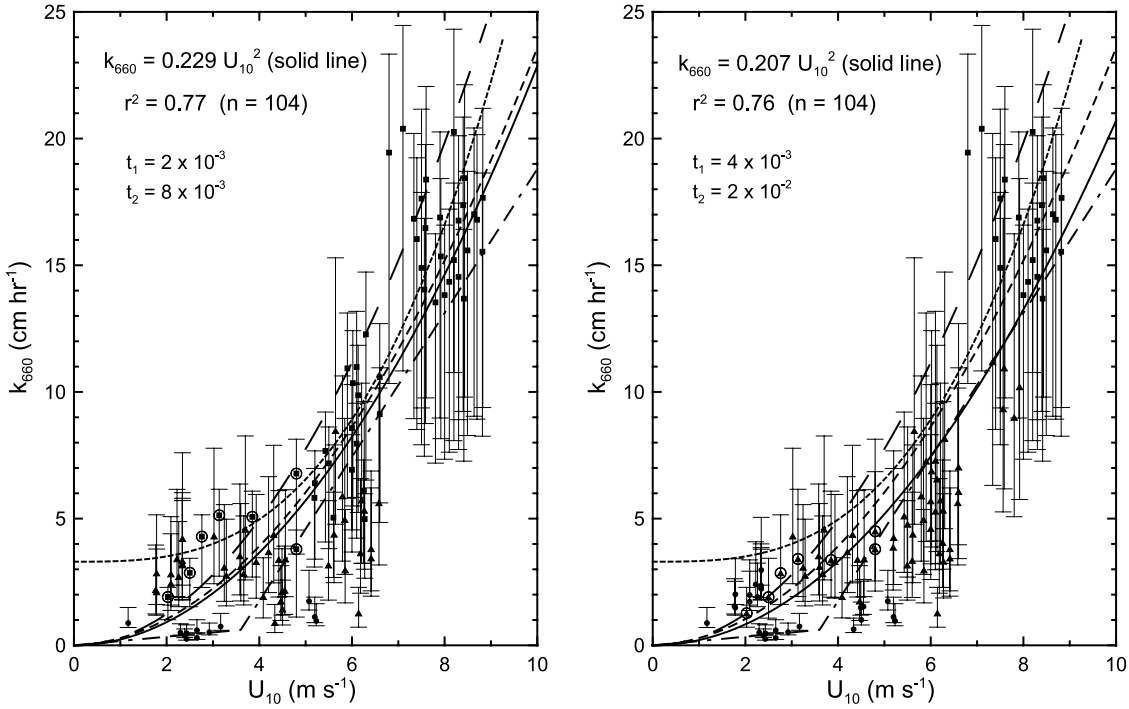

Figure 4. Gas transfer velocity k_{660} versus U_{10} for two alternate Schmidt number scaling scenarios (see text): (left) t_1 = 2E−03 and t_2 = 8E−03 and (right) t_1 = 4E−03 and t_2 = 2E−02, along with best fit lines and $k_{660} - U_{10}$ relationships as in Figure 3. Solid circles, k_{660} (n = 0.67); solid triangles, k_{660} (n = 0.59); solid squares, k_{660} (n = 0.5). Circled points represent rain events.

DCFS consisted of a Solent three-axis ultrasonic anemometer-thermometer, an Ophir infrared hygrometer, and a Systron-Donner MotionPak system of three orthogonal angular rate sensors and accelerometers. The MotionPak was mounted directly beneath the sonic anemometer, which allowed accurate alignment with the sonic axes in addition to ensuring that the wind and motion measurements were collocated. An infrared hygrometer/CO_2 sensor developed by NOAA/ATDD at Oak Ridge was added to the flux system for CoOP97.

[18] A more complete description of the DCFS, including an analysis of the ship-induced flow distortion, is given by *Edson and Fairall* [1998]. On the *Oceanus*, the DCFS system was deployed on the forward jack staff directly above the bow. This placed the anemometer 17 m above the mean sea surface. The corrected velocity components from these relative wind directions were used to compute the momentum, gas, sensible heat, and water vapor fluxes using the direct covariance method. For example, the momentum, sensible heat, and latent heat fluxes are defined as

$$\tau = \rho_a \overline{u'w'}, \tag{3}$$

$$Q_s = \rho_a c_{pa} \overline{w'T'}, \tag{4}$$

$$Q_l = \rho_a L_e \overline{w'q'}, \tag{5}$$

respectively, where ρ_a is the density of air, c_{pa} is the specific heat of air, L_e is the latent heat of evaporation, u' and w' are the fluctuating longitudinal and vertical wind velocity components, respectively, and T' and q' are the fluctuation temperature and specific humidity, respectively. Friction velocities were directly measured with eddy correlation as

$$u_{*a} = \left(-\overline{u'w'}\right)^{1/2}. \tag{6}$$

Flux estimates were also computed from the bulk flux algorithm described by *Fairall et al.* [1996]. Radiative heat fluxes were determined using radiometers mounted on the forward jack staff and the infrared bow package. The net heat flux was calculated as the sum of the radiative, sensible, and latent heat fluxes. A more complete description of the meteorological measurements made during CoOP97 is given by *Edson et al.* [1999].

[19] The 10-m wind speed used in our analysis has been corrected to neutral conditions using Monin-Obukhov (MO) similarity theory [e.g., *Edson and Fairall*, 1998]. The correction, which attempts to remove the effects of atmospheric stability, is given by

$$U_N(z) = U(z) + \frac{u_*}{\kappa}\psi_m\left(\frac{z}{L}\right), \tag{7}$$

where κ is the von Karman's constant, ψ_m is the stability function for momentum, and L is the MO length. The stability functions described by *Fairall et al.* [1996] were used in the analyses and we used a value of 0.4 for the von Karman's constant.

3.4. Wave Measurements

[20] Small-scale wave measurements were made using a scanning laser slope gauge [*Bock and Hara*, 1995] mounted on a frame extending forward from the bow of LADAS.

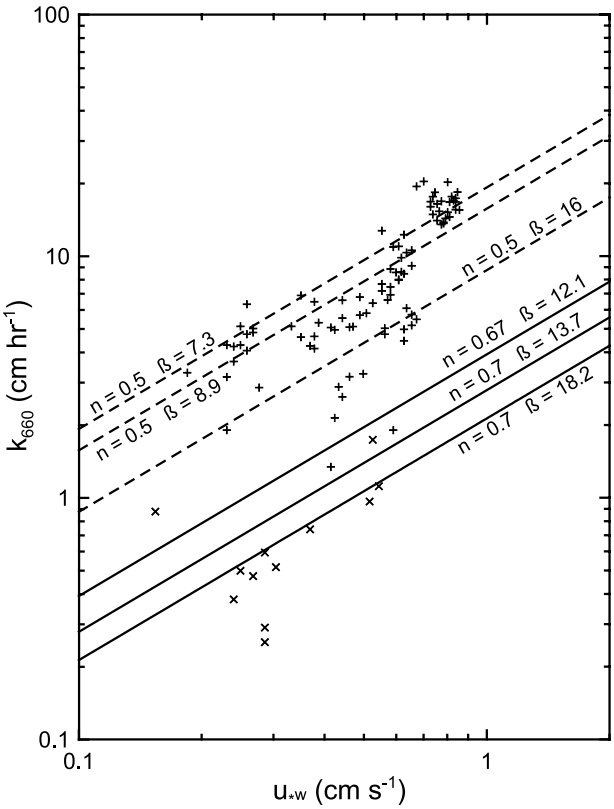

Figure 5. Gas transfer velocity k_{660} versus water-side friction velocity $u_{*}w$. Various model lines calculated from equation (8) are shown for comparison (pluses are nonslicked, n = 0.5; crosses are slicked, n = 0.67).

During deployment, LADAS was remotely piloted directly into the wind to avoid distortion of the wave field. The slope gauge provided full three-dimensional frequency–wave number spectra from 40–800 rad m^{-1} for an undisturbed patch of water. The data are reported here as the one-sided, directionally integrated surface slope spectrum $S(\kappa)$, the degree of saturation $B(\kappa) = S(\kappa)\,\kappa^2$ and mean square slope $\langle S^2 \rangle = \int S(\kappa)\,\kappa d\kappa$ integrated over four wave number ranges: 40–100, 100–200, 200–400, and 400–800 rad m^{-1}. All data have been averaged over a minimum of 10 min so that the estimated error is less than 10%.

3.5. Microlayer Surface Chemical Enrichments

[21] The sea surface was sampled continuously with a surface microlayer skimmer (SMS) designed by *Carlson et al.* [1988]. The SMS consisted of a partially submerged, rotating glass cylinder supported by a small catamaran, which acted as a wave follower. The rotating cylinder collected a thin layer of water (40–60 μm thickness) by viscous retention. The theoretical basis for the sampling mechanism has been described by *Levich* [1962] and experimentally verified by *Cinbis* [1992]. The sampler was nested within the hulls of the LADAS catamaran directly behind the scanning laser slope gauge so that surface film concentrations could be compared with surface roughness on virtually the same patch of sea surface. The sampler produced a 100 mL min^{-1} flow of microlayer water; a second sampling line supplied subsurface water from a nominal depth of 10 cm. Both flow streams were routed to a fluorometry package mounted on LADAS.

[22] Colored dissolved organic matter (CDOM) was used as a proxy for surfactants in seawater. It is important to note that, while CDOM fluorescence has been shown to correlate strongly with surfactants in seawater, CDOM is a limited proxy for surfactants because it does not include many classes of naturally occurring nonchromophoric and insoluble surfactants. Also, seasonal and regional variations in the relationship between CDOM fluorescence and seawater surfactants are observed [*Frew et al.*, 2002], suggesting variability in the composition or proportion of surface active compounds in the CDOM pool.

[23] CDOM fluorescence was measured using a Turner Designs 10-AU field fluorometer equipped with a 25 mm path length, continuous flow quartz cell. The excitation wavelength was 355 nm; the emission wavelength was 450 nm. Fluorescence was calibrated using quinine sulfate as a standard. One fluorescence unit (F.U.) was set equal to the fluorescence of a one part per billion quinine sulfate solution

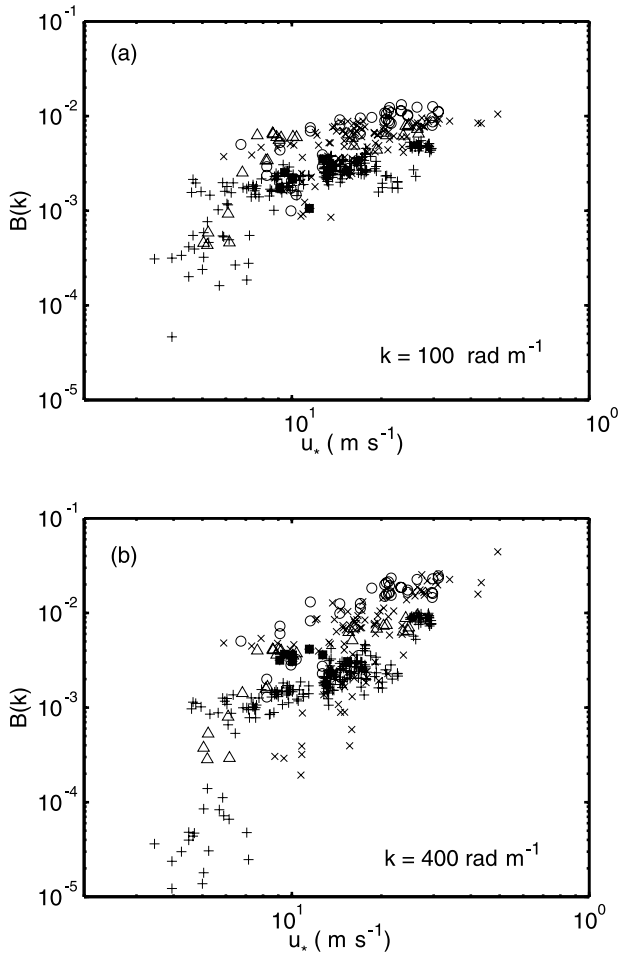

Figure 6. Degree of saturation $B(\kappa)$ of short wind waves versus air-side friction velocity u_{*a} at wave numbers (a) κ = 100 rad m^{-1} and (b) κ = 400 rad m^{-1}. Pluses are from CoOP97, solid squares are from CoOP97 during rain events, crosses are from off the California coast during CoOP95 [*Hara et al.*, 1998], circles are from off Cape Hatteras [*Hara et al.*, 1998], and triangles are from off Martha's Vineyard [*Hara et al.*, 1994].

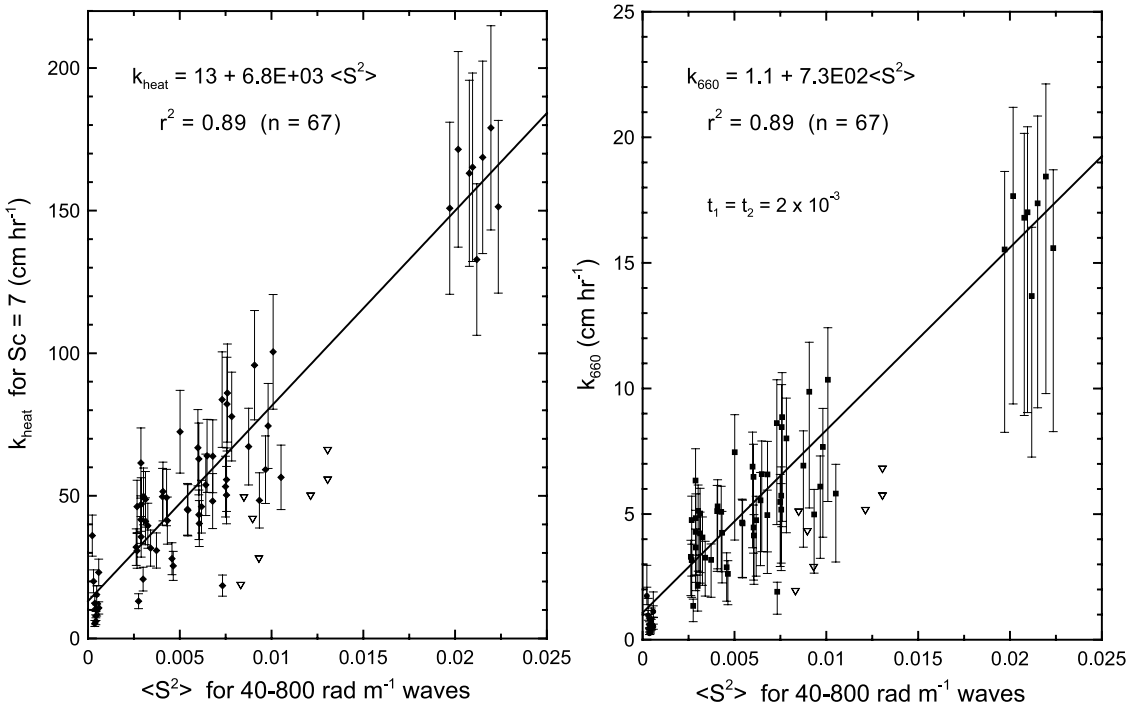

Figure 7. (left) Heat transfer velocity k_{heat} and (right) gas transfer velocity velocity k_{660} versus mean square slope $\langle S^2 \rangle$ for the wave number range 40–800 rad m^{-1}: solid diamonds, unscaled k_{heat}; solid circles, k_{660} ($n = 0.67$); and solid squares, k_{660} ($n = 0.5$). Schmidt number exponents used to scale k_{heat} to k_{660} were assigned using mean square slope criterion $t_1 = t_2 = 2E{-}03$ (see text). Solid lines are linear best fits for 67 data pairs ($k_{heat} = 13 + 6.8 \times 10^3 \langle S^2 \rangle$, $r^2 = 0.89$; $k_{660} = 1.1 + 7.3 \times 10^2 \langle S^2 \rangle$, $r^2 = 0.89$). Inverted triangles represent data collected during rain events not included in best fit calculations.

(1 ppb q.s.) [*Vodacek et al.*, 1997]. In order to provide surface enrichment estimates, a single fluorometer was used to measure surface microlayer and subsurface fluorescence alternately over 8- and 2-min intervals, respectively.

3.6. Ancillary Measurements

[24] Chlorophyll was measured using a WetLabs WETStar fluorometer mounted on the shipboard continuous flow seawater line. The WETStar response was calibrated using discrete GF/F filtered seawater samples and coproporphyrin methyl ester as a standard. Other chemical parameters were measured on discrete samples taken either from the ship's flow line or from a second SMS deployed on a small boat. Dissolved organic carbon (DOC) was measured by a high temperature catalytic oxidation method [*Peltzer and Brewer*, 1993]. Surface-active organic matter (SAOM) was measured by a polarographic method using Triton X-100 as a standard [*Hunter and Liss*, 1980] and is reported in mg L^{-1} of Triton-X-100. Salinity and sea surface temperature were taken from the ship's SAIL system.

4. Results and Discussion

4.1. Wind Speed Dependence of Gas Transfer Velocity

[25] Analysis of the CoOP97 thermal imagery resulted in 104 heat transfer velocity estimates. (Appendix 1, containing the complete data set, is provided as auxiliary material[1]). Although estimates of ΔT from the infrared imager were made on very short timescales (O 10 s), the temporal resolution of the transfer velocity estimates was limited by the meteorological net heat flux estimates, which required averaging over 15 minute intervals to reduce uncertainty. The estimates of k_{heat} and k_{660} (as 15 minute averages in units of cm hr^{-1}) are shown in Figure 3 as functions of U_{10} averaged over the same interval. The wind speed dependence of k_{heat} is described by a quadratic relationship (solid line in Figure 3 (left)): $k_{heat} = 2.33U_{10}^2$, (coefficient of determination $r^2 = 0.76$ for 104 data pairs). The observed dependence of k_{660} on wind speed is also nonlinear and can be best described by a quadratic relationship (solid line in Figure 3 (right)) that accounts for 75% of the variance: $k_{660} = 0.239U_{10}^2$. In this case, mean square slope thresholds $t_1 = t_2 = 2E{-}03$ were used to derive k_{660}. The gas transfer velocity-wind speed relationships of *Wanninkhof* [1992] (long-dashed line), *Liss and Merlivat* [1986] (dash-dotted line), and *McGillis et al.* [2001a] (short-dashed line) are also plotted for reference. The extrapolation of heat transfer velocities to Sc = 660 yields gas transfer velocities that are in general agreement with estimates derived by other methods. Overall, the wind speed dependence obtained by fitting the CoOP97 data is nearly identical to that obtained by *Nightingale et al.* [2000b] by fitting the results from several dual tracer release experiments: $k_{600} = 0.24U_{10}^2 + 0.061U_{10}$. The latter relationship, adjusted to k_{660} ($k_{660} = 0.228U_{10}^2 + 0.058U_{10}$), is also plotted (medium-dashed line) in Figure 3. The majority of the estimates of k_{660} derived from the thermal imagery fall within the general envelope

[1]Auxiliary material is available at ftp://ftp.agu.org/apend/jc/2003JC002131.

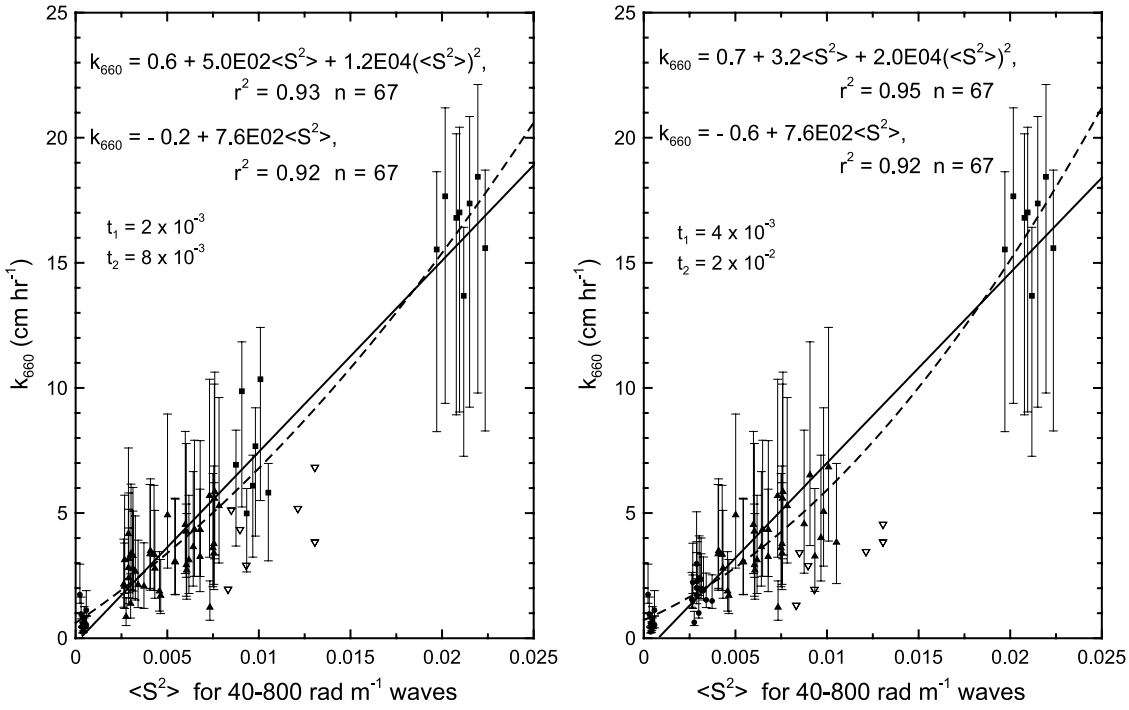

Figure 8. Gas transfer velocity k_{660} versus mean square slope $\langle S^2 \rangle$ for two alternate Schmidt number scaling scenarios (see text): (left) t_1 = 2E−03 and t_2 = 8E−03 and (right) t_1 = 4E−03 and t_2 = 2E−02, along with linear (solid) and quadratic (dash) best fit lines for 67 data pairs. Solid circles, k_{660} (n = 0.67); solid triangles, k_{660} (n = 0.59); and solid squares, k_{660} (n = 0.5). Inverted triangles represent rain events not included in best fit calculations.

defined by the idealized relationships for wind speeds above 6 m s^{-1}. However, for wind speeds less than 6 m s^{-1}, most of the points lie outside this envelope and are poorly predicted by wind speed in this range.

[26] The error bars for k_{heat} reflect an overall uncertainty of ∼20–25%, which includes an uncertainty of ∼15% arising from the combined heat flux error and the estimation of ΔT from the observed temperature distribution (based on the laboratory comparisons made by *Schimpf et al.* [2004]), and the variability of the ΔT values within the 15-min averaging interval. Error bars for the gas transfer rate reflect the additional uncertainty of the Schmidt number scaling from the heat transfer velocity to Sc = 660, depending on the scaling scenario as described above. Roughly 25% of the observations were significantly impacted by surface films and are over predicted by the Wanninkhof and Nightingale relationships for wind speed 0–7 m s^{-1}, whereas the Liss-Merlivat relationship overpredicts ∼12% of the observations for winds in the range of 5–7 m s^{-1}. Interestingly, for nearly all of the observations classified as 'slicked' (solid circles), the k_{660} estimates were actually quite low and consistent with (or lower than) the low and moderate wind segments of the Liss-Merlivat transfer velocity-wind speed relationship; this may suggest that the underlying ΔT values were not grossly underestimated by the thermographic technique. Observations made during light to heavy rain (circled points) tend to lie slightly above the best fit line.

[27] In Figure 4, k_{660} is shown as a function of U_{10} for the cases where the Schmidt number scaling has been implemented with two alternate mean square slope threshold criteria. For the case in which t_1 = 2E−03 and t_2 = 8E−03 (Figure 4 (left)), the wind speed dependence is described by a quadratic function, $k_{660} = 0.23U_{10}^2$ with slightly improved fit (r^2 = 0.77) and for the case in which t_1 = 4E−03 and t_2 = 2E−02 (Figure 4 (right)), the wind speed dependence is also described by a quadratic function, $k_{660} = 0.21U_{10}^2$, with r^2 = 0.76. As expected, transfer velocities calculated at low wind speeds using the alternate threshold criteria are visibly depressed relative to those shown in Figure 3. However, the fitted curves do not change significantly, given the uncertainty in the individual data points. Thus the choice of Schmidt number exponent using the different thresholding schemes does not have a major effect on the basic quadratic relationship between transfer velocity and wind speed.

4.2. Wind Stress Dependence of Gas Transfer Velocity

[28] The gas transfer velocity is more fundamentally related to wind stress than wind speed, and thus is frequently modeled in terms of the Schmidt number and the water-side friction velocity u_{*w}:

$$k = \beta^{-1} Sc^{-n} u_{*w}, \tag{8}$$

where $u_{*w} = u_{*a}\,(\rho_a/\rho_w)^{0.5}$ and ρ_w is the water density. The coefficient β is the dimensionless transfer resistance for gas transfer [*Jähne et al.*, 1987a]. The Schmidt number exponent n is related to the boundary condition for water-side turbulence at the interface [*Ledwell*, 1984; *Jähne*, 1985; *Jähne et al.*, 1987b]. For the limiting case of gas transfer at a smooth rigid wall, *Deacon*'s [1977] theoretical treatment

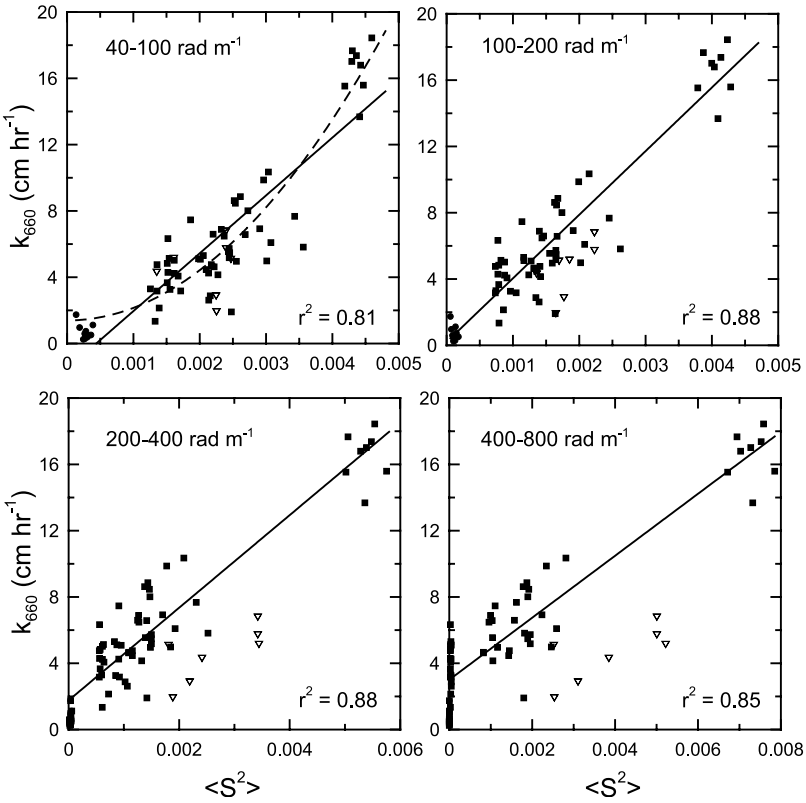

Figure 9. Gas transfer velocity k_{660} versus mean square slope $\langle S^2 \rangle$ for selected wave number ranges (κ = 40–100, 100–200, 200–400, and 400–800 rad m^{-1}). Schmidt number exponents used to scale k_{heat} to k_{660} were assigned using mean square slope criterion $t_1 = t_2 = 2E{-}03$ (see text). Symbols are as defined in Figure 8. Linear fit lines (solid) and coefficients of determination are shown. A quadratic fit (dash) to the data for κ = 40–100 rad m^{-1} is also shown ($r^2 = 0.87$). Rain event data (inverted triangles) were excluded from all fit calculations.

yielded $n = 0.67$ and $\beta = 12.1$. *Münnich and Flothmann* [1975] developed a similar expression for a free wavy surface based on a surface renewal model [*Danckwerts*, 1970] and predicted $\beta = 16$ and $n = 0.5$. *Jähne et al.* [1987a] derived somewhat different values from experimental work in wind-wave flumes of different scales, obtaining $\beta = 13.7$ and $n = 0.7$ for a surface covered with surface films and $\beta = 8.9$ and $n = 0.5$ for a clean surface.

[29] In Figure 5, the CoOP97 estimates of k_{660} are plotted as a function of u_{*w}. The scatter in the data is quite large and reflects a wave field-dependent transition between limiting transport regimes. The logarithmic format facilitates comparison of model curves (equation (8)) representing various estimates of the two limiting transport regimes (rigid wall and free surface models). The default thresholding scheme ($t_1 = t_2 = 2E{-}03$) used for Figure 5 essentially separates the data into two groups: nonslicked and slicked surfaces. The former represent free surfaces that are marked by the presence of small-scale waves; these nevertheless may be influenced by the presence of surface films as indicated by small CDOM enrichments. The slicked data group represents cases of extreme surface film accumulation, distinguished by very low surface slope values ($\langle S^2 \rangle_{\kappa=40-800} < 2 \times 10^{-3}$) and high CDOM enrichments (typically ΔCDOM > 0.1 ppb q.s.). The k_{660} data for slicked surfaces generally lie near but slightly below the theoretical and experimentally determined lines for transfer at a rigid wall and are roughly linear with u_{*w}. The discrepancy between the CoOP97 data and the *Jähne et al.* [1987a] model line with $\beta = 13.7$ may simply reflect a small bias in the transfer velocity measurement at these low levels. Taking them at face value and assuming $n = 0.7$, a fit to these data yields $\beta = 18.2$. For cases of nonslicked (but possibly film-influenced) surfaces, the increase in k_{660} with u_{*w} is greater than linear and the data clearly are not well represented by equation (8) using a unique set of constants β and n. Transfer velocities at a given friction velocity are enhanced by up to an order of magnitude relative to those measured for slicked surfaces, consistent with numerous studies in laboratory wind-wave tanks that show significant enhancement of gas transfer with the development of small-scale waves [e.g., *Broecker et al.*, 1978; *Jähne et al.*, 1987a; *Frew et al.*, 1995; *Frew*, 1997]. Some of this enhancement is explained by a change in the Schmidt number dependence. The influence of surface films on gas transfer via viscoelastic damping of turbulence and waves is known to be significant [*Frew et al.*, 1995; *Frew*, 1997]. As in laboratory studies, the presence of surface films during the CoOP97 experiment are likely to have influenced the degree of wave-induced exchange enhancement and this possibility will be examined later in this paper. A subset of the data for which $u_{*w} > 0.7$ cm s^{-1} (Figure 5) exhibits significantly higher k_{660} than would be predicted from equation (8) using the *Jähne et al.* [1987a] estimates of n and β for a free

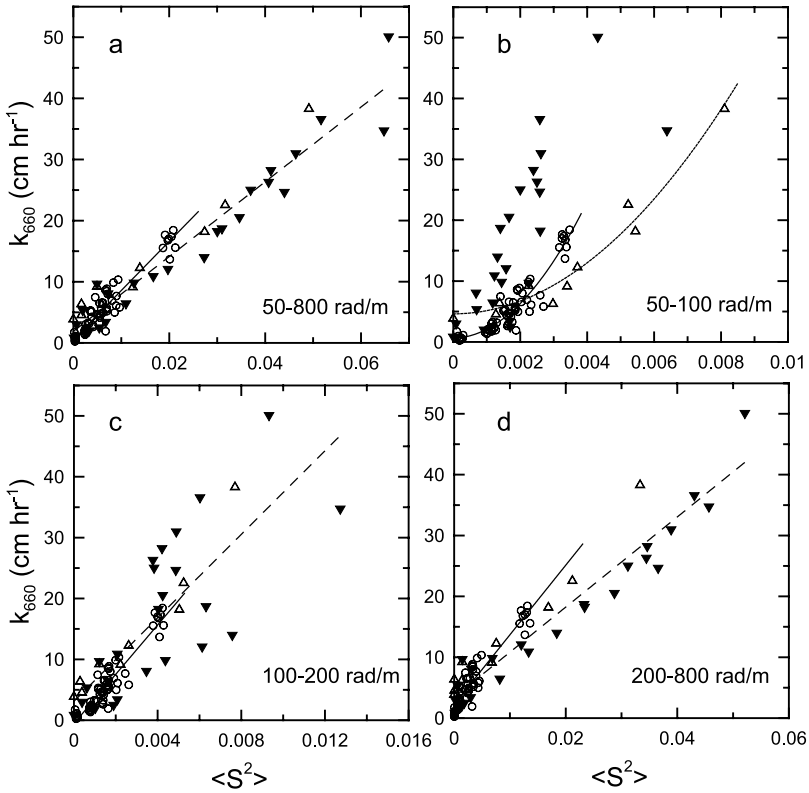

Figure 10. Comparison of mean square slope dependence of gas transfer velocity for field and wave tank observations (open circles, CoOP97; solid inverted triangles, WHOI 0.5 m diameter annular tank [*Frew et al.*, 1995]; and open triangles, UH 4 m diameter annular tank [*Bock et al.*, 1999]). Fit lines for CoOP97 (linear, solid), WHOI + UH (linear, dash), and UH only (quadratic, dot) are also shown to show trends.

surface with waves. These data also correspond to the lowest surface film enrichments observed in the field experiment and may represent an approach to 'clean surface' conditions. If, for reasons discussed later in the section on surfactants, these are taken as a limiting (nonviscoelastic) case for surface renewal, then a new model curve can be added to Figure 5 corresponding to n = 0.5 and β = 7.3.

4.3. Small-Scale Wave Spectra

[30] The degree of saturation $B(\kappa)$ at wave numbers κ = 100 rad m^{-1} and 400 rad m^{-1} from the CoOP97 experiment is plotted versus u_{*a} (pluses) in Figure 6. Data obtained during rain events at station 5 (yearday 192) are differentiated from nonrain events using solid squares. The results are compared with previous field observations shown with various symbols in Figure 6. Overall, the CoOP97 results are within the scatter (but closer to the lower bound, particularly for κ = 100 rad m^{-1}) of previous observations. The degree of saturation $B(\kappa)$ at κ = 100 rad m^{-1} depends weakly (less than linear) on u_{*a} while $B(\kappa)$ at κ = 400 rad m^{-1} depends strongly on u_{*a}. The degree of saturation $B(\kappa)$ at κ = 400 rad m^{-1} shows larger variability (more than two orders of magnitude) at lower friction velocities, suggesting that shorter waves are more strongly affected by surface films. The data for rain events in CoOP97 show some enhancement of $B(\kappa)$ over the other CoOP97 data at κ = 400 rad m^{-1}, but the rain event data are not enhanced at κ = 100 rad m^{-1}. The CoOP97 data include extremely low values of $B(\kappa)$ at low friction velocities due to surface films. Even the results at κ = 100 rad m^{-1} are significantly reduced. Since the CoOP97 data exhibit particularly large variability of the short wave spectrum at a given friction velocity, this data set presents an excellent opportunity to investigate the dependence of the transfer velocity on surface roughness and to compare the result with the dependence on the wind speed and wind stress as discussed in sections 4.1 and 4.2.

4.4. Mean Square Slope Dependence of Gas Transfer Velocity

[31] The gas transfer velocities computed from heat transfer velocities allow examination of potential relationships between transfer velocity, mean square slope and surface film enrichment. First, the mean square slope dependence of the transfer velocity is explored by examining correlations between k_{660} and $\langle S^2 \rangle$, where $\langle S^2 \rangle$ is obtained by integrating the omnidirectional wave number slope spectrum $S(\kappa)$ [*Bock et al.*, 1999] over the full wave number range measured (κ = 40–800 rad m^{-1}). This range corresponds to wavelengths between 0.79 cm and 16 cm. The result thus differs from the 'total' mean square slope in that it excludes slope contributions from gravity waves longer than ~16 cm and capillary waves shorter than 0.79 cm. On the basis of previous laboratory observations, the contribution of capillary waves shorter than 0.79 cm

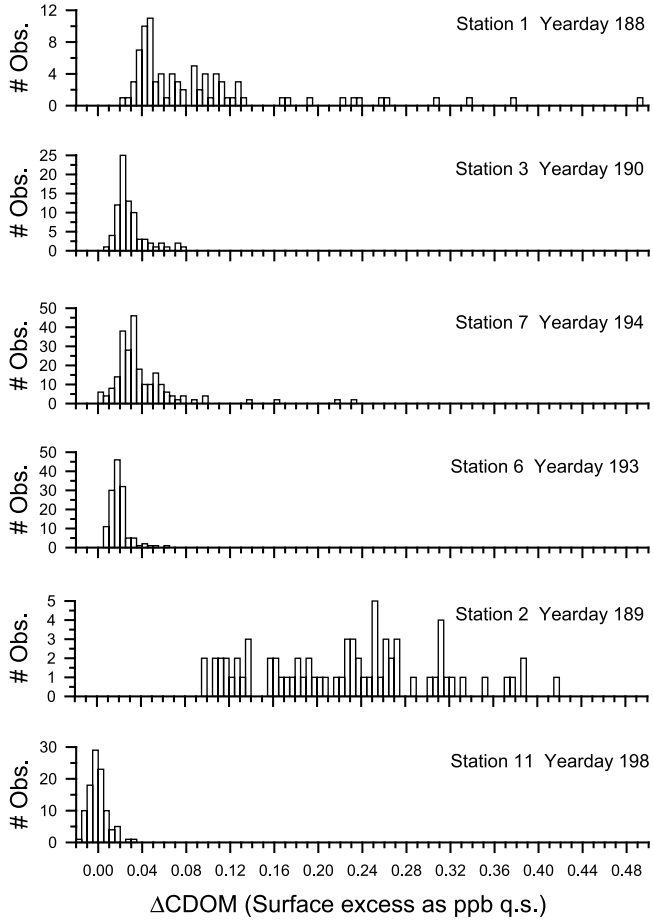

Figure 11. Histograms of ΔCDOM distributions for six CoOP97 stations. See Figure 1 and Table 1 for locations and ancillary chemical and physical data. The surface excess CDOM (ΔCDOM) is defined as the difference between the CDOM fluorescence in the microlayer (50 μm nominal sampling depth) and that in the subsurface water (10 cm nominal depth) and is reported as a concentration difference in parts per billion quinine sulfate (ppb q.s.).

to the mean square slope is estimated to be less than 20%.

[32] Of the 104 transfer velocity measurements, 74 had both corresponding slope and surface film data; of these, 7 were influenced by rain events and are treated separately. Figure 7 presents (left) k_{heat} and (right) k_{660} versus $\langle S^2 \rangle$ for the resulting 67 data pairs. Mean square slope threshold values $t_1 = t_2 = 2E{-}03$ were used to compute k_{660}. The data suggest a linear dependence on $\langle S^2 \rangle$ computed for this wave number range. The linear best fit relationship for heat is $k_{heat} = 13 + 6.8 \times 10^3 \langle S^2 \rangle$, $r^2 = 0.89$ and that for gas is $k_{660} = 1.1 + 7.3 \times 10^2 \langle S^2 \rangle$, $r^2 = 0.89$. Some of the remaining variance may be due to small-scale variability in surface film distributions (see section 4.5.2), since the thermal imagery and slope measurements were not spatially collocated (typically 0.5 km separation). Observations made during rain events are clearly anomalous and are significantly overpredicted by the best fit relationship.

[33] In Figure 8, k_{660} is shown as a function of $\langle S^2 \rangle$ where the Schmidt number assignments were made using the two alternate mean square slope threshold criteria, analogous to Figure 4. Both linear and quadratic best fit lines are shown. The linear fits yielded small negative intercepts, whereas the quadratic fits yielded small positive intercepts and gave slightly higher coefficients of determination ($r^2 = 0.93$ for $t_1 = 2E{-}03$ and $t_2 = 8E{-}03$ (Figure 8 (left)), and $r^2 = 0.95$ for $t_1 = 4E{-}03$ and $t_2 = 2E{-}02$ (Figure 8 (right)). As with the relationships derived for $k_{660} - U_{10}$, the apparent $k_{660} - \langle S^2 \rangle$ relationships were not particularly sensitive to the choice of threshold values used to assign values to n. Predicted transfer velocities at $\langle S^2 \rangle = 0.025$ differed by only ~10% for the different scaling schemes and these differences were well within the estimated error limits. The coefficients of determination for correlations with mean square slope were significantly larger than those obtained for correlations with wind speed when curve fits (quadratic) were performed for the same 67 data pairs. Versus wind speed, these latter coefficients were, for k_{heat}, $r^2 = 0.71$ and for k_{660}, $r^2 = 0.70$, 0.76, and 0.78 respectively, for the three thresholding schemes.

[34] The relative contribution of various wave scales to the transfer velocity dependence on slope can be examined in more detail by integrating the slope spectrum over selected wave number ranges as presented in Figure 9. The wave number-binned data indicate that there is generally a strong correlation between k and $\langle S^2 \rangle$ at all wave numbers above 40 rad m^{-1} ($r^2 \geq 0.85$). For $\kappa = 40{-}100$ rad m^{-1}, the transfer velocity variation with slope appears to be slightly nonlinear. While one could argue, given the uncertainty, that the relationship is basically linear, it is best fitted with a quadratic function ($k_{660} = 1.4 + 7.58 \times 10^5 (\langle S^2 \rangle)^2$, $r^2 = 0.87$). The slope dependence becomes essentially linear for $\kappa > 100$ rad m^{-1}. Another interesting feature of the data is that their distribution along the best fit lines becomes increasingly bimodal as the wave number range increases. A pronounced rolloff in the mean square slope is observed with increasing wave number for the majority of the data pairs relative to a cluster of high slope points which, as pointed out in section 4.2, correspond to an ocean surface relatively uncontaminated by surface films. The implication is that the slope spectrum in the high wave number region is being modulated by surfactants.

[35] Data collected during rain events at station 5 (yearday 192) diverge from the general trend (Figure 9). In the wave number range 40–100 rad m^{-1}, where raindrops do not contribute to enhanced slope, the transfer velocity–mean square slope data pairs follow the same relationship as the nonrain data pairs. In the higher wave number ranges, however, the impact of raindrops on the ocean surface contributes to the mean square slope. Interestingly, there appears to be no correspondingly strong enhancement in the gas transfer velocity. The rain data fall increasingly below the trend line with increasing wave number. *Ho et al.* [2000] observed significant enhancement of gas transfer by rain in freshwater systems due to the additional turbulence generated by drop impacts, but found that surface slope due to ring waves was not well correlated with transfer velocity when data for different drop sizes were considered. The observations made during rain in this study are only slightly elevated relative to nonrain observations when considered as a function of U_{10} (Figures 3 and 4). One explanation might be that development of an overlying thin freshwater

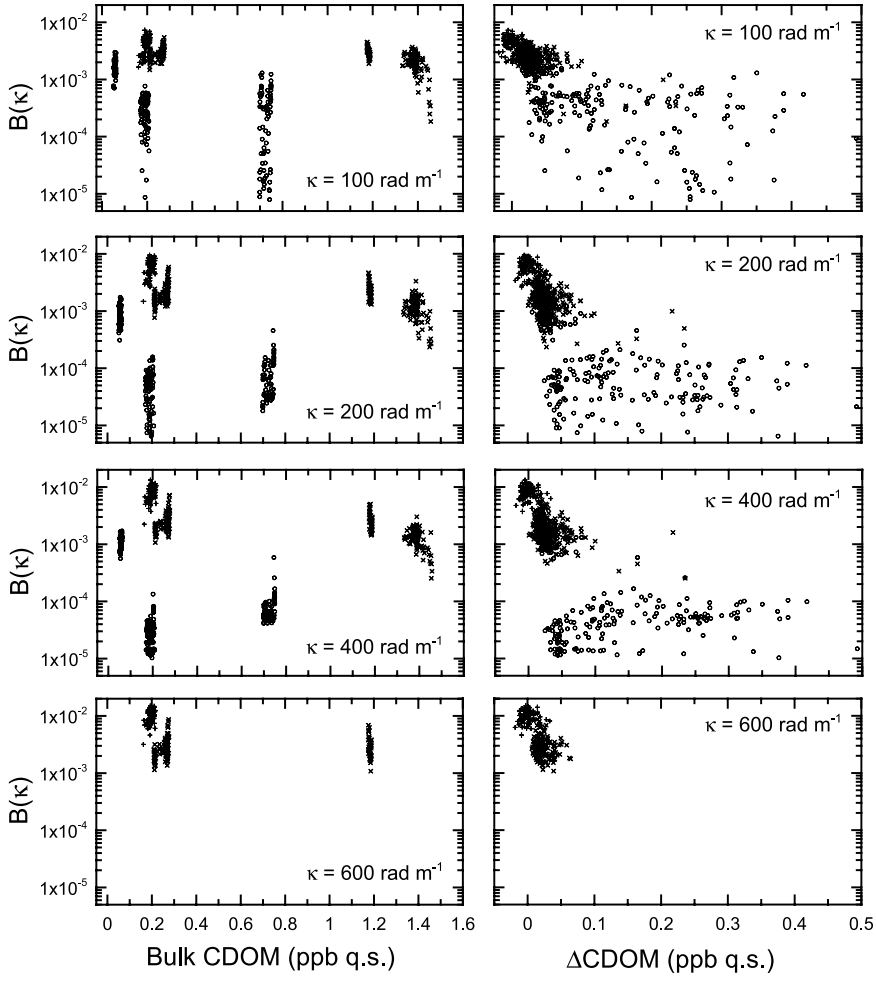

Figure 12. Degree of saturation $B(\kappa)$ versus near-surface (10 cm depth) (left) CDOM and (right) ΔCDOM in units of ppb q.s. for all available CoOP97 data pairs at four different wave numbers: $\kappa = 100$, 200 and 400 and 600 rad m^{-1}. Symbols differentiate different wind stress levels: plus, $0.2 < u_{*a} < 0.4$ m s^{-1}; cross, $0.1 < u_{*a} < 0.2$ m s^{-1}; circle, $0.05 < u_{*a} < 0.1$ m s^{-1}.

layer during an oceanic rain event inhibits surface renewal due to buoyancy effects. Also, a dramatic increase in ΔCDOM (Table 1) was observed during the rain showers. It was not possible to determine whether the increase was due to washout of an interfering chemical species or due to additional surface-active materials from wet deposition or release of CDOM from lysing cells. A third possibility is simply that the assumptions involved in deriving the transfer velocities from the thermal imagery using the surface renewal model break down during rain events and that a different model would need to be developed for rain conditions.

[36] In Figure 10, the dependence of the in situ transfer velocity on the mean square slope is compared with the laboratory results reported by *Bock et al.* [1999]. The in situ mean square slope has been recalculated over the same wave number ranges as the laboratory results, so that direct comparisons are possible. (Note however, that the upper wave number limit of the laboratory results was approximately 1200 rad m^{-1}, whereas the CoOP97 results only extend to 800 rad m^{-1}. As discussed earlier, this difference does not affect the mean square slope values by more than 20%.)

[37] The dependence of k_{660} on the mean square slope integrated from 50 to 800 rad m^{-1} (>50 rad m^{-1} for laboratory results) is roughly consistent between the field and laboratory results (Figure 10a). The field transfer velocities are slightly higher than the laboratory results at a given mean square slope. This difference may be due to the fact that the mean square slope of the field results does not include the contribution from wave numbers above 800 rad m^{-1}. The dependence of the transfer velocity on relatively longer surface waves, mean square slope integrated over 50–100 rad m^{-1} (Figure 10b) or 100–200 rad m^{-1} (Figure 10c), exhibits significantly more scatter compared to the dependence on shorter waves (200–800 rad m^{-1}) shown in Figure 10d. This is mainly because laboratory wave fields over the wave number range of 50–200 rad m^{-1} are strongly influenced by the tank geometry [*Bock et al.*, 1999].

4.5. Influence of Surface Films

[38] In this section, observations of surfactant distributions made during the experiment are summarized. Hydrodynamic modulation of surface waves, near-surface turbulence, and surface renewal by surfactant films is well

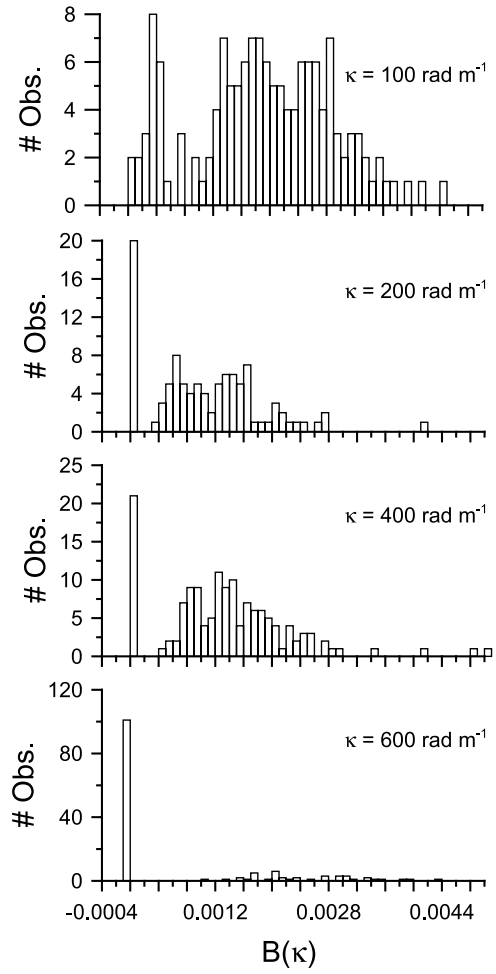

Figure 13. Histograms of degree of saturation $B(\kappa)$ for CoOP97 observations with low ΔCDOM (0.025–0.045 ppb q.s.) showing $B(\kappa)$ attenuation at high wave numbers.

established [see *Frew*, 1997]. An important objective of the CoOP97 experiment therefore was to assess the influence of surfactants on gas transfer over a range of wind and sea state conditions and over a range of spatial scales.

4.5.1. Large-Scale Surface Film Variations

[39] On large spatial scales (10–1000 km), differences in biological production of surface-active materials, for example, in eutrophic coastal waters as compared to oligotrophic waters, might be expected to govern the occurrence, extent and concentration of surfactant films. Although slicks are widely observed in both coastal and open waters [*Stewart*, 1985], *Romano* [1996] has provided statistics showing that slicks are more frequent in coastal waters than in open ocean waters, on the basis of photographic observations along cruise tracks in Mediterranean Sea, Red Sea, and Indian Ocean. *Nilsson and Tildesley* [1995] concluded from their interpretation of ERS-1 synthetic aperture radar (SAR) imagery that, apart from wind effects, the largest variations in SAR backscatter (1–10 dB) are associated with different water masses with different levels of surface-active materials. In an annular laboratory wind-wave facility, *Frew* [1997] demonstrated that transfer velocities measured at the same wind speed using seawater samples collected along a coastal-offshore transect increased systematically as organic matter levels decreased.

[40] While those experiments demonstrated the potential of varying SAOM levels to modulate transfer velocities, it was not clear that this mechanism would dominate in situ. Numerous processes driven by wind potentially contribute to variable film distributions in situ, and the effects of local wind stress could well dominate over bulk seawater surfactant concentration in determining in situ surface film concentrations. If the wind stress is sufficiently low for an extended period, surface enrichment can occur even in low-latitude, oligotrophic regions where DOC concentrations, although low, are nevertheless sufficient to support film formation [*Hühnerfuß et al.*, 1977]. At moderate to high wind stress, breaking waves disrupt the surface and physically drive film components back into the bulk seawater. Relatively soluble film components may desorb back into bulk solution with increasing straining of the sea surface by wind waves. The rate at which films are advected horizontally away from their source (the surface drift velocity is typically 3–4% of the wind speed) competes with the rate of surfactant supply from the subsurface via diffusion and vertical advection. The recent history of the wind forcing is also likely to be important in that the processes of accumulation and erosion of surface films lag changes in wind stress.

[41] Although the present data set is too sparse to examine these issues definitively, some tentative conclusions can be drawn by comparing results from individual stations. In Figure 11, we present histograms showing the distribution of ΔCDOM observations during six individual LADAS deployments. Ancillary data on bulk seawater organic matter concentrations, including DOC, SAOM, and CDOM, and the average wave slope $S(\kappa)$ at several wave numbers can be found in Table 1. The histograms are arranged according to average wind speed for each deployment. First, we consider the concentration gradients represented by stations 7, 1, and 3 or 7, 6, and 3. The records for station 1 (yearday 188) and station 3 (yearday 190) show quite different ΔCDOM distributions for nearly identical average wind conditions ($U_{10} \approx 2.5$ and 2.1 m s^{-1}, respectively). Film concentrations were generally higher and more broadly distributed at station 1 than at station 3, consistent with higher subsurface concentrations at the former station. Conversely, the average $S(\kappa)$ for κ = 400 rad m^{-1} at station 1 was lower than that for station 3 by a factor of 35 (Table 1). The transfer velocity was about ninefold lower at station 1. A comparison of data from stations 6 and 7 ($U_{10} \approx 4.2$ m s^{-1}) again shows that, under similar wind conditions, ΔCDOM and average $S(\kappa)$ are respectively higher and lower at the site with the higher bulk organic matter concentrations (station 7). The average transfer velocity at station 7 is only 60% of the average observed at station 6. The area sampled at station 1 was revisited ten days later (station 11) when higher winds prevailed ($U_{10} \approx 8.5$ m s^{-1}). At that time, although the levels of DOC and CDOM were comparable to the earlier period, the average microlayer CDOM showed no statistically significant enrichment over the subsurface water (ΔCDOM ≈ 0) and the average wave slope was higher by over two orders of magnitude. Thus both the surface film enrichment and wave slope tend to be more strongly influenced by wind than by

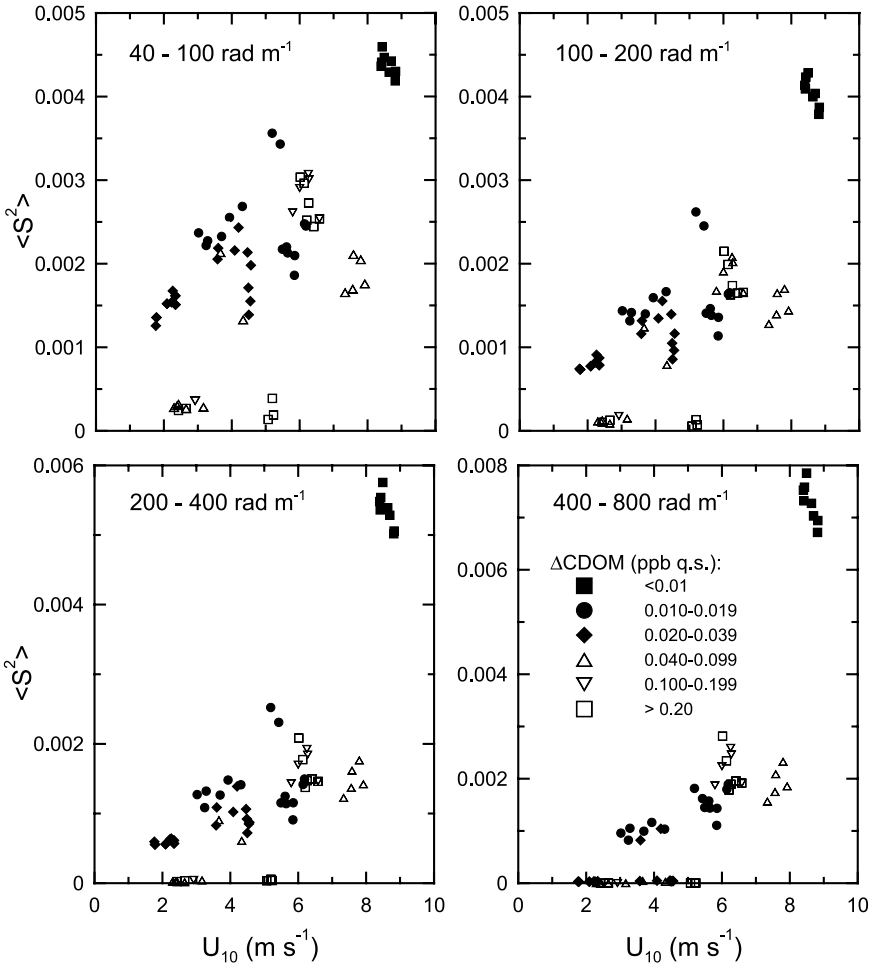

Figure 14. Mean square slope $\langle S^2 \rangle$ versus wind speed U_{10}, binned by wave number range and distinguished by different ΔCDOM levels (see legend).

bulk organic matter concentration. However, the broad distribution and relatively high levels of ΔCDOM observed at station 2 (Figure 11) illustrate that no simple rule relating ambient film accumulation to bulk concentration and wind speed can be formulated. Despite 5 m s^{-1} average winds, millpond conditions prevailed at this productive site on Georges Bank. Organic matter levels, although high, were comparable to the other coastal sites studied (stations 7 and 8). The concentrated slicks observed at this station may reflect a lag in the dispersion of surfactant materials accumulated during a preceding period of light winds. Alternatively, they may reflect active upwelling that commonly occurs on Georges Bank, potentially accelerating the adsorption rate at the interface and creating convergence zones.

[42] The six records in Figure 11 suggest that regions of high bulk surfactant concentration tend to have higher surface film concentrations and lower wave slope at a given wind speed than regions of low bulk organic matter concentrations, but that surface film concentrations drop sharply with increasing wind speed as expected. *Nightingale et al.* [2000b] measured gas transfer velocities in the Southern Ocean during the progression of a bloom stimulated by iron fertilization. They reported no significant difference between prebloom and bloom gas transfer velocities, as determined from dual tracer (SF_6/^{3}He) releases in steady prevailing winds of 6–8 m s^{-1}. Although no surface film or surfactant measurements were made, it appears likely based on our observations that differences in film accumulations at these wind speeds would be minimal and that any resulting small reductions in transfer velocity due to surfactants during the bloom would be very difficult to detect using their methodology.

[43] Since surface films are subject to multiple physical processes that redistribute or erode them in competition with processes that form them from the ambient bulk DOC, it is unlikely that their impact on gas transfer velocities can be predicted from bulk organic matter concentrations or estimates of phytoplankton abundance (e.g., DOC or chlorophyll). This is in contrast to earlier observations in wave tanks [*Frew*, 1997] under tightly controlled forcing conditions where many of the aforementioned mechanisms were not operative.

[44] A related observation is that wave slope is more clearly dependent on ΔCDOM than CDOM or other measures of bulk organic matter concentrations or phytoplankton abundance (e.g., DOC and chlorophyll levels). Hydrodynamic modulation of the wave field (and near-surface turbulence) by surfactants requires surface tension gradients generated during surface straining by excess organic material at the interface. This is explored further

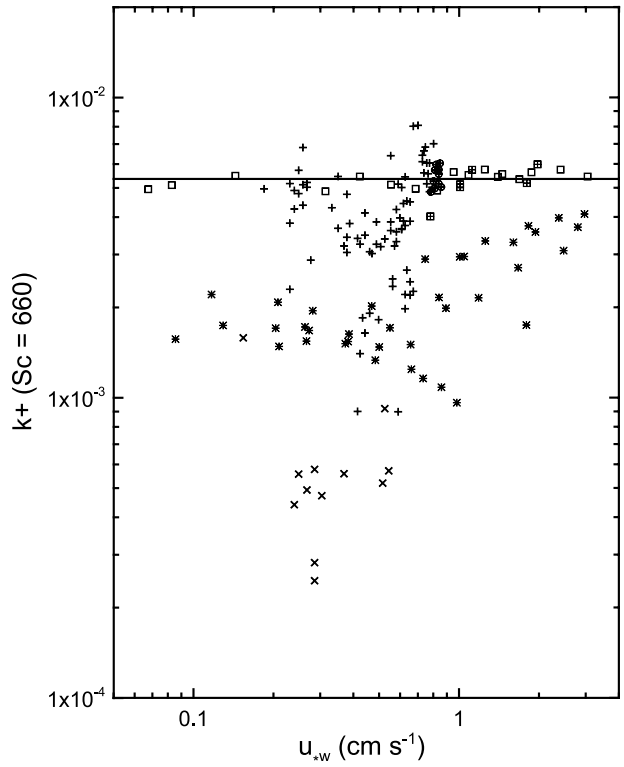

Figure 15. Dimensionless gas transfer velocity ($k_+ = k_{660}/u_{*w}$) versus water-side friction velocity u_{*w}: open squares, WHOI clean surface; square with plus, UH clean surface; star, UH with surfactant; plus, CoOP97 nonslicked; cross, CoOP97 slicked; circle w/plus, CoOP97 station 11 (yearday 198). Solid line is the fit to WHOI clean surface data [*Frew et al.*, 1995].

in Figure 12 which shows the degree of saturation, $B(\kappa) = \kappa^2 S(\kappa)$, as a function of bulk CDOM and ΔCDOM. The data cover a range of wind stress levels as denoted by different symbols. It is clear from Figure 12 that there is no correlation between $B(\kappa)$ and CDOM. The very lowest and highest values of $B(\kappa)$ observed during the CoOP97 experiment occur at virtually the same low CDOM levels concentration levels. Further, moderately high $B(\kappa)$ are observed at the highest CDOM levels. In contrast, clear trends are apparent in Figure 12, when $B(\kappa)$ levels at κ = 100, 200, 400 and 600 rad m^{-1} are compared with ΔCDOM. The degree of saturation is strongly reduced as surface enrichment levels increase. $B(\kappa)$ decreases more slowly with increasing ΔCDOM at 100 rad m^{-1} than at 200 or 400 rad m^{-1}. The influence of ΔCDOM is most pronounced at low wind stress levels ($u_{*a} < 0.1$ m s^{-1}), where $B(\kappa)$ is highly variable and may be suppressed by up to two orders of magnitude.

[45] It is difficult to separate the effects of wind stress and ΔCDOM on $B(\kappa)$ more definitively without reference to an 'abiotic', surfactant-free ocean. However, we can make further deductions regarding surfactant influences on gas transfer by examining the high wave number region of the slope spectrum. Theoretical formulations of wave damping in the presence of viscoelastic films predict that the introduction of a small finite viscoelastic modulus impacts the high wave number region of the slope spectrum most strongly [*Lucassen-Reynders and Lucassen*, 1969; *Lucassen-Reynders*, 1986; *Cini et al.*, 1987; *Bock and Mann*, 1989]. As viscoelasticity increases, the damping phenomenon affects waves of increasingly lower wave number. Recent measurements of the slope spectra of wind-driven waves in laboratory tanks reported by *Bock et al.* [1999] confirm this phenomenon. They found that at high wave numbers, $B(\kappa)$ remained roughly constant or increased slightly with wave number for wind waves generated on very clean water but decreased dramatically at high wave numbers with the introduction of very low levels of surfactants. Suppression of $B(\kappa)$ progressed to longer waves as surfactant levels increased. Thus, if low surfactant (surface excess) levels are modulating wave slope in the oceanic environment, we should see similar behavior of $B(\kappa)$ with respect to ΔCDOM at high κ.

[46] The wave number–binned mean square slope data of Figure 9 show that spectral levels at high wave numbers are strongly correlated with gas transfer velocity. Thus, if waves at the smallest scales can be shown to be attenuated by surface films, then we can deduce that the transfer velocity will also be lower than would be expected for an uncontaminated sea surface with a viscoelastic modulus that approaches zero. In Figure 13, we present histograms of $B(\kappa)$ at wave numbers 100, 200, 400 and 600 rad m^{-1} for all of the CoOP97 data where ΔCDOM was between 0.025 and 0.045 ppb q.s. The $B(\kappa)$ distributions for κ > 100 rad m^{-1} become narrower and shift toward lower mean $B(\kappa)$. At κ = 600 rad m^{-1}, very few observations exhibit nonzero (i.e., above the noise level of the instrument) $B(\kappa)$. Thus, even low surface film concentrations appear to be affecting surface roughness at high wave numbers.

[47] This is examined further in Figure 14 where $\langle S^2 \rangle$ is plotted versus U_{10} for the same wave number bins as in Figure 9. The data symbols indicate the degree of surface film enrichment as measured by excess CDOM. Moving from low to high wave number bins, mean square slope decreases systematically at a given wind speed for the majority of the observations. Qualitatively, the degree to which $\langle S^2 \rangle$ is suppressed corresponds to the level of ΔCDOM, particularly at low wind speeds. The suppression of mean square slope becomes more pronounced as wave number increases. Thus, the waves of smallest scale are

Figure 16. Photo taken from bow of R/V *Oceanus* of the LADAS catamaran traveling along the axis of a banded slick at station 7 (yearday 194).

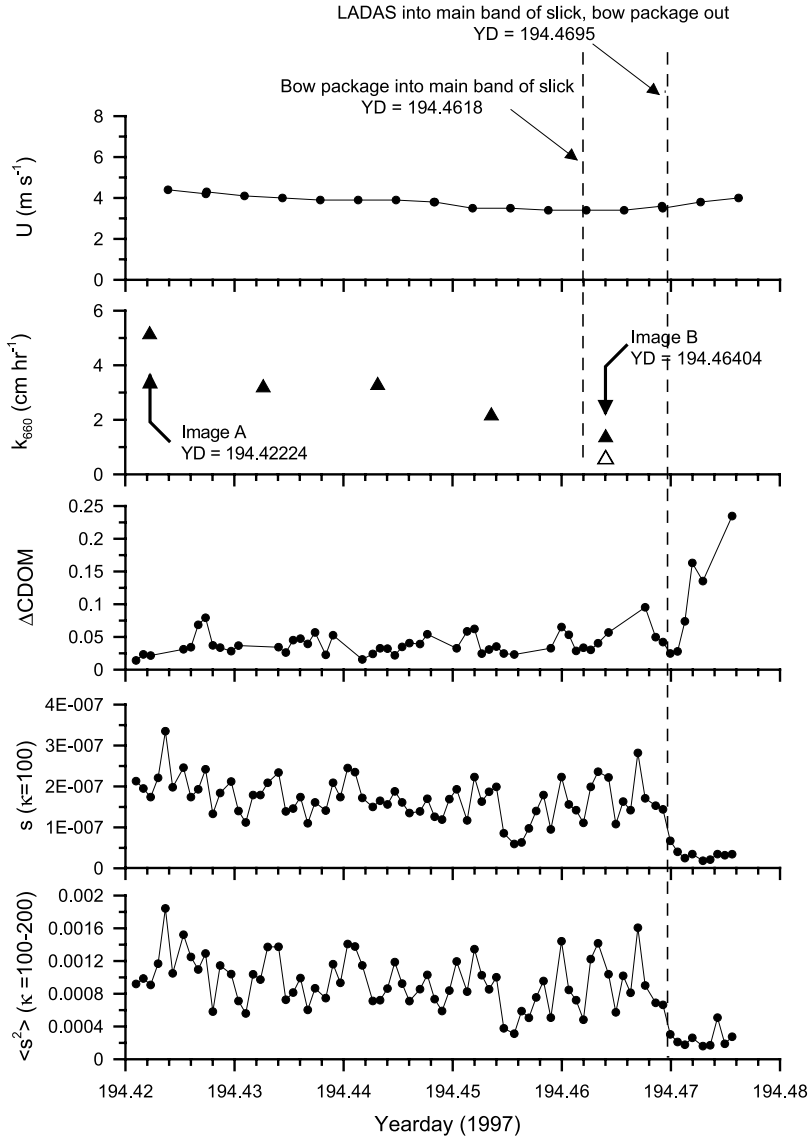

Figure 17. Time series of U_{10} and k_{660} derived from the bow package on *Oceanus* and ΔCDOM, S at $\kappa = 100$ rad m^{-1}, and $\langle S^2 \rangle \kappa = 100-200$ rad m^{-1} from LADAS during deployment at station 7 (yearday 194). Maneuvers (see text) placed the bow package footprint in the heaviest slick band beginning at YD = 194.4618, while LADAS entered the band at 194.4695. The record shows a decrease in k_{660} within the slick relative to that observed outside the slick at the beginning of the record; k_{660} values were calculated using $n = 0.5$ for Schmidt number scaling (solid triangles) and $n = 0.67$ (open triangle).

most sensitive to the wave damping effect of surface films, as predicted by theory. Mean square slopes computed for the 'cleanest' air-sea interface encountered during the CoOP97 experiment (station 11 (yearday 198), black squares in Figure 14) are the least impacted and remain well separated from most of the other data.

[48] Finally, the field data are compared with previously reported laboratory results [*Frew et al.*, 1995] using equation (8), which predicts that k should vary linearly with u_{*w}. Figure 15 shows the dimensionless transfer velocity $k_+ = k/u_{*w}$ plotted versus u_{*w} for data from the small WHOI annular tank, the UH annular tank and the CoOP97 field experiment. Of these, only the WHOI tank 'clean surface' data maintain the predicted constant k_+ down to very low u_{*w}. Most of the other measurements only begin to approach the average of the WHOI tank k_+ observations (represented by the solid line) when u_{*w} approaches 0.6–0.7 cm s^{-1}. The WHOI tank 'clean surface' measurements were carried out under conditions of extremely low adventitious surface film contamination [*Frew et al.*, 1995]. *Scott* [1972, 1975] clearly demonstrated that the 'critical wind speed' for the generation of capillary ripples, often observed in wind-wave tank experiments, is an artefact that is highly dependent on the degree of surface contamination. He found no evidence of a critical wind speed for the initiation of wind waves on assiduously cleaned water surfaces. The WHOI tank 'clean surface' results supported Scott's observations in that capillary waves were observed for u_{*w} as low as 0.07 cm s^{-1}. In contrast, the UH tank 'clean surface' results showed a decline in k_+ below $u_{*w} = 1.0$ cm s^{-1}.

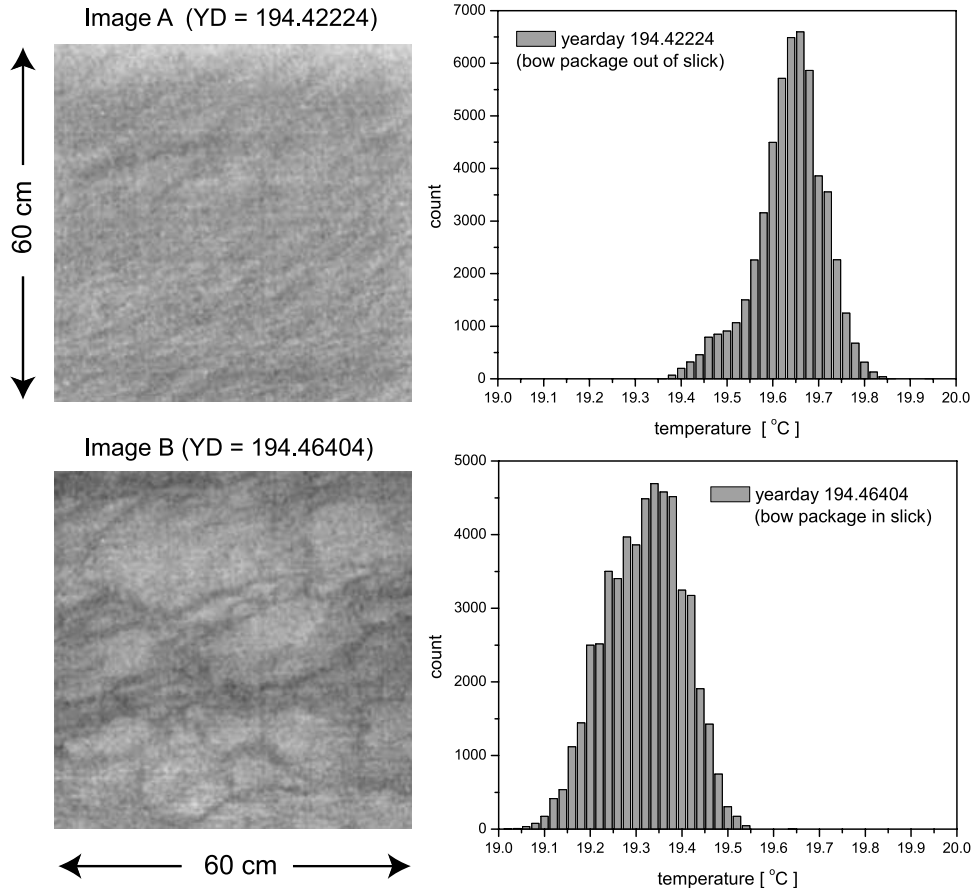

Figure 18. Comparison of thermal images and derived temperature histograms at two discrete times in the yearday 194 time series (see Figure 17): image A, bow package footprint outside main slick at 194.42224, and image B, bow package footprint in main slick at 194.46404.

Since truly clean surfaces were difficult to achieve in the UH tank because of its large water volume and surface area, residual adventitious surfactants were effective in depressing gas transfer rates below this wind stress level. Similarly, the CoOP97 results generally fall below the WHOI tank 'clean surface' results. However, the subset of CoOP97 observations mentioned previously as representing 'clean' sea surface (station 11, shown as encircled pluses in Figure 15) fall on this line in close agreement with the WHOI and UH tank data for 'clean' surfaces. A number of other observations from deployments at the oligotrophic stations (stations 3 and 4) also lie near or slightly above this line, suggesting relatively clean sea surfaces. Although DOC, SAOM or CDOM data are not available for station 4, it is reasonable to expect values as low as those at station 3 since the two stations were nearly collocated. The data of Figures 12–15 provide the most direct evidence to date that surfactant films modulate in situ gas transfer for winds below 7–8 m s^{-1} by modifying small-scale roughness.

4.5.2. Small-Scale Surface Film Variations

[49] On small spatial scales (10–1000 m), the patchiness of surface film distributions due to variations in localized forcing, upwelling, surface convergences and divergences, tidal flows, wave-current interactions and buoyant overturning should be reflected in the local wave slope, the frequency of surface renewal, and the transfer velocity. Examples of small-scale variability have been presented previously [*Frew et al.*, 2002] in which microlayer and subsurface CDOM fluorescence records clearly showed complex patterns of enrichments on the ocean surface ranging in scale from tens to hundreds of meters. This small-scale variability has also been shown previously to be negatively correlated with wave slope [*Frew et al.*, 2002]. The surface film effect on gas transfer velocity can now be directly examined by comparing IR images, wave slope and ΔCDOM measurements made outside and within one of these small-scale surface features. Figure 16 is a photo of such a feature taken from the bow of the R/V *Oceanus* at station 7 (yearday 194). Most of the record at this station showed relatively low ΔCDOM, but several banded slicks with heavy film concentrations were also encountered during the deployment. The photo shows the LADAS catamaran traveling along the axis of a banded slick, which was oriented in a northeast-southwest direction. From the sunglint pattern, it is apparent that LADAS was located in the most concentrated slick region, while the ship was traveling in a less heavily filmed region.

[50] A series of maneuvers was conducted to test the effect of the surface film on gas transfer velocity. The ship, with its bow-mounted infrared imager, was piloted gradually into and along this banded feature from the south

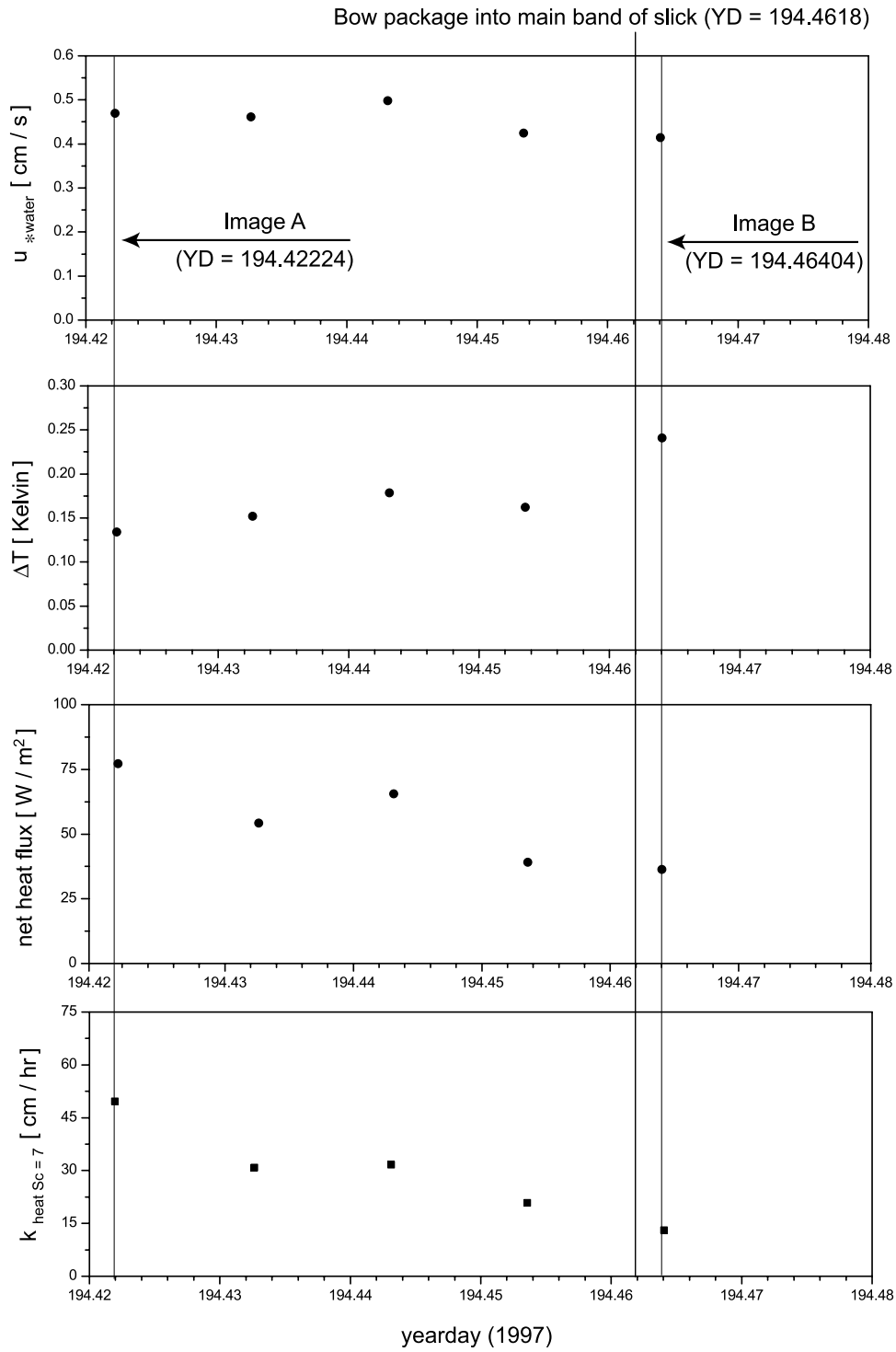

Figure 19. Yearday 194 time series of the water-side friction velocity, (u_{*w}), surface temperature gradient (ΔT), net heat flux (j_{heat}), and heat transfer velocity (k_{heat}), showing that the decrease in k_{heat} and thus k_{660} (see Figure 17) within the slick band was due to a combined increase in ΔT of ~80% and a decrease in the heat flux of ~50%.

(foreground in photo). The bow package acquired images of the heaviest part of the slick beginning at ~194.462, continuing for ~15 min. Subsequently, LADAS, which had been traveling outside and parallel to the band, was steered into the slick at ~194.469, approaching it from a position north of the heavy band, crossing a relatively sharp boundary (evident from the photo). Figure 17 presents the time series of bow and LADAS observations (U_{10}, k_{660}, S, $\langle S^2 \rangle$, and ΔCDOM) preceding and during these operations. It is important to note that the bow observations (U_{10} and k) are slightly separated in time and space from the LADAS observations (S, $\langle S^2 \rangle$, and ΔCDOM), but that both the

Oceanus and LADAS instruments sampled the same persistent surface film within a 20-min window.

[51] The record from the bow instruments shows that U_{10} varied between 4.4 m s^{-1} and 3.5 m s^{-1}, with a slight downward trend until ~194.465 and then increasing again to 4.1 m s^{-1}. The gas transfer velocity decreased from 5.1 cm h^{-1} at the beginning of the record to 1.3 cm h^{-1} during the period within the heavy band, assuming a Schmidt number exponent $n = 0.5$. If $n = 0.67$ is used to scale k_{heat} for the observation within the slick band, as seems more appropriate given the high ΔCDOM and low $S(\kappa)$, then k_{660} is calculated to be only 0.64 cm h^{-1}. The records from the LADAS instruments suggest a slight increasing trend in ΔCDOM until ~194.469, then a sharp increase as LADAS entered the band, while the wave slope S at $\kappa = 100$ rad m^{-1} and the mean square slope $\langle S^2 \rangle$ for $\kappa = 100-200$ rad m^{-1} mirrored this, decreasing slowly and undergoing a strong attenuation at ~194.469.

[52] Figure 18 compares two infrared images taken by the thermal imager on the bow package at 194.42224 and 194.46404 (see Figure 17). Image A was acquired when the R/V *Oceanus* was outside the slicked area, whereas image B was recorded while the ship traveled through the main band of the slick. During the timeframe where the two images were recorded, the data from the bow instruments show that the friction velocity varied between 0.47 cm s^{-1} and 0.42 cm s^{-1} with a slight downward trend of about 5% (Figure 19). At the same time, the estimated temperature gradient increased from 0.13 Kelvin to 0.24 Kelvin and the net heat flux dropped from 77.2 Watt m^{-2} to 36.5 Watt m^{-2}. The increase of about 80% in the temperature gradient and the decrease of the net heat flux (roughly 50%) leads to a significant drop of the heat transfer velocity calculated using equation (1) from 49.7 cm h^{-1} to 13.1 cm h^{-1} (Figure 19) while the slick was present. Image B from the heavy film band shows larger spatial scales of the temperature fluctuation at the sea surface and larger ΔT (see Figure 18) characteristic of reduced surface renewal at the interface and an attenuation of mixing in the aqueous boundary layers. Similar results were reported from laboratory studies carried out by *Schimpf et al.* [2004]. They showed that in the presence of a surfactant film, near-surface turbulence is suppressed leading to an increase in the temperature gradient across the thermal boundary layer accompanied by a shift from small to large-scale surface temperature fluctuations.

5. Conclusions

[53] Gas transfer velocities extrapolated from heat transfer velocities measured during the CoOP97 experiment generally fall within the bounds of commonly used transfer velocity-wind speed relationships and follow a quadratic relationship with U_{10} that is similar to one derived by *Nightingale et al.* [2000b]. The quadratic relation explains ~75% of the observed variance with respect to wind and, like previous relationships, significantly overpredicts transfer velocities in situations where concentrated surface films are present. The field data encompass winds only up to 10 m s^{-1} and thus do not constrain the likely dependence at higher wind speeds.

[54] The dependence on wind stress as represented by u_{*w} is also found to be nonlinear with considerable scatter, reflecting a wave field-dependent transition between limiting transport regimes. Application of previous models derived by *Münnich and Flothmann* [1975] and *Deacon* [1977] for free wavy and rigid surfaces respectively, suggests that these models are not adequate to describe gas transfer in the presence of surface films and that both n and β are likely to depend on wave slope or other roughness parameters.

[55] Gas transfer velocity is found to vary linearly with mean square slope obtained by integrating the slope spectrum $S(\kappa)$ over the full wave number range measured (40–800 rad m^{-1}). The derived linear relationship explains roughly ~89% of the observed variance and does not overpredict transfer velocity in the presence of surface films. The relationship with slope becomes nonlinear with alternate assumptions about the Schmidt number dependence, explaining 93–95% of the variance. Deviations from linearity are also observed when various wave number subranges are examined. In all cases, however, $\langle S^2 \rangle$ is a better predictor of transfer velocity than either U_{10} or u_{*w}.

[56] Surface films monitored by measuring the elevated fluorescence from surface-active CDOM at the air-sea interface clearly reduce wave slope and therefore reduce gas transfer velocities. The reduction in wave slope is particularly pronounced at high wave numbers. Wave slope and gas transfer velocities are not well correlated with large-scale variations in bulk organic matter concentration due mainly to the action of disruptive wind-driven physical processes, which compete with film formation by diffusion from the bulk and which strongly affect film distributions. Wave slope and transfer velocity are strongly correlated with actual surface chemical enrichment, however, as represented in this work by ΔCDOM.

[57] The small-scale wave field is influenced by multiple factors. These include among others, the wind stress and its time history, fetch-dependent wave age, wave-wave and wave-current interactions, atmospheric boundary layer stability and surface films. Thus, at any given wind speed, an infinite variation of sea state is possible. This suggests that a better approach to parameterizing gas transfer would be to use surface roughness directly, i.e., to focus on the net effect of these combined factors in setting the ambient sea state. The CoOP97 results generally corroborate our previous conclusion from laboratory studies that parameterization of gas transfer velocity using the mean square slope of small-scale waves could result in more consistent gas flux estimates when compared to simple wind speed parameterizations. Furthermore, surface roughness, specifically mean square slope, can be sensed using the same space-based microwave devices (altimeters and scatterometers) that provide wind speed measurements. Thus parameterizations using mean square slope or other roughness indicators could provide more accurate regional- and global-scale assessments of the transfer velocity field. We note that, from a remote sensing point of view, the shortest waves may not be the best choice to monitor gas transfer remotely since they disappear so quickly with the advent of surface films. Waves in the 40–100 rad m^{-1} range may be a more reasonable compromise between persistence and sensitivity to changes in forcing or to surface films. Last, we reemphasize the caveats that the observations in this study were limited to low and moderate wind conditions and that the

passive flux technique used to estimate transfer velocities was not sensitive to bubble-mediated processes other than bubble-generated turbulence. Extrapolation of the results to high wind conditions is thus not recommended.

[58] **Acknowledgments.** Funding for this work was provided by the NSF Coastal Ocean Processes (CoOP) program (OCE-9410534, OCE-9711285 (WHOI) and OCE-9409222, OCE-9711391(URI)). Additional support for data analysis was provided by NASA (NAGW-2431, JPL Contract 961425). Partial funding was also provided by the German Science Foundation (DFG) through the DFG research unit FOR240: Image Sequence Analysis to Investigate Dynamic Processes. The authors wish to thank W. Witzell, Jr. and D. Schroeder of the Woods Hole Oceanographic Institution for their role in the design, construction, and deployment of the LADAS catamaran. We also thank the officers and crew of the R/V *Oceanus* for their competent assistance and patience during the CoOP97 cruise. We note sadly that this is a posthumous contribution from our friend and colleague, Dr. Erik J. Bock, who passed away in June 2001, and whose effort and ingenuity made the CoOP97 experiment a success. This is Contribution No. 11187 of the Woods Hole Oceanographic Institution.

References

Agrawal, Y. C., E. A. Terray, M. A. Donelan, P. A. Hwang, A. J. Williams III, W. M. Drennan, K. K. Kahma, and S. A. Kitaigorodskii (1992), Enhanced dissipation of kinetic energy beneath surface waves, *Nature*, *359*, 219–220.

Asher, W. E., and J. F. Pankow (1989), Direct observation of concentration fluctuations close to a gas/liquid interface, *Chem. Eng. Sci.*, *44*, 1451–1455.

Asher, W. E., and J. F. Pankow (1991), The effect of surface films on concentration fluctuations close to a gas/liquid interface, in *Gas Transfer at Water Surfaces*, edited by S. C. Wilhelms and J. S. Gulliver, pp. 68–79, Am. Soc. of Civ. Eng., New York.

Bock, E. J., and T. Hara (1995), Optical measurements of capillary-driven wave spectra using a scanning laser slope gauge, *J. Atmos. Oceanic Technol.*, *12*, 395–403.

Bock, E. J., and J. A. Mann Jr. (1989), On ripple dynamics. II. A corrected dispersion relation for surface waves in the presence of surface elasticity, *J. Colloid Interface Sci.*, *129*, 501–505.

Bock, E. J., et al. (1995), Description of the science plan for the April, 1995 CoOP experiment, "Gas Transfer in Coastal Waters," performed from the Research Vessel *New Horizon*, in *Air-Water Gas Transfer*, edited by B. Jähne and E. Monahan, pp. 801–810, AEON, Hanau, Germany.

Bock, E. J., T. Hara, N. M. Frew, and W. R. McGillis (1999), Relationship between air-sea gas transfer and short wind waves, *J. Geophys. Res.*, *104*, 25,821–25,831.

Broecker, H. C., J. Petermann, and W. Siems (1978), The influence of wind on CO_2–exchange in a wind-wave tunnel, including the effects of monolayers, *J. Mar. Res.*, *36*, 595–610.

Carlson, D. J., J. L. Cantey, and J. J. Cullen (1988), Description of and results from a new surface microlayer sampling device, *Deep Sea Res., Part A*, *35*, 1205–1213.

Cinbis, C. (1992), Noncontacting techniques for measuring surface tension of liquids, *E. L. Ginzton Lab. Rep. 4931*, Stanford Univ., Stanford, Calif.

Cini, R., P. P. Lombardini, C. Manfredi, and E. Cini (1987), Ripple damping due to monomolecular films, *J. Colloid Interface Sci.*, *119*, 74–80.

Csanady, G. T. (1990), The role of breaking wavelets in air-sea gas-transfer, *J. Geophys. Res.*, *95*, 749–759.

Danckwerts, P. V. (1951), Significance of liquid-film coefficients in gas absorption, *Ind. Eng. Chem.*, *43*, 1460–1467.

Danckwerts, P. V. (1970), *Gas-Liquid Reaction*, McGraw-Hill, New York.

Davies, J. T. (1970), *Turbulence Phenomena*, Academic, San Diego, Calif.

Deacon, E. L. (1977), Gas transfer to and across an air-water interface, *Tellus*, *29*, 363–374.

Donelan, M. A., and R. Wanninkhof (2002), Gas transfer at water surfaces—Concepts and issues, in *Gas Transfer at Water Surfaces*, *Geophys. Monogr. Ser.*, vol. 127, edited by M. A. Donelan et al., pp. 1–107, AGU, Washington, D. C.

Drennan, W. M., M. A. Donelan, E. A. Terray, and K. B. Katsaros (1996), Oceanic turbulence dissipation measurements in SWADE, *J. Phys. Oceanogr.*, *26*, 808–815.

Edson, J. B., and C. W. Fairall (1998), Similarity relationships in the marine atmospheric surface layer for terms in the TKE and scalar variance budgets, *J. Atmos. Sci.*, *55*, 2311–2328.

Edson, J. B., A. A. Hinton, K. E. Prada, J. E. Hare, and C. W. Fairall (1998), Direct covariance flux estimates from mobile platforms at sea, *J. Atmos. Oceanic Technol.*, *15*, 547–562.

Edson, J. B., W. R. McGillis, and N. M. Frew (1999), Atmospheric forcing and energy exchange during the 1997 CoOP gas exchange experiment, Extended Abstracts, paper presented at 13th Symposium on Boundary Layers and Turbulence, Am. Meteorol. Soc., Dallas, Tex.

Erikson, D. J., III (1993), A stability dependent theory for air-sea gas exchange, *J. Geophys. Res.*, *98*, 8471–8488.

Fairall, C. W., E. F. Bradley, D. P. Rogers, J. B. Edson, and G. S. Young (1996), Bulk parameterization of air-sea fluxes for TOGA COARE, *J. Geophys. Res.*, *101*, 3747–3764.

Fairall, C. W., J. E. Hare, J. B. Edson, and W. R. McGillis (2000), Parameterization and micro-meteorological measurement of air-sea transfer, *Boundary Layer Meteorol.*, *96*, 63–105.

Frew, N. M. (1997), The role of organic films in air-sea gas exchange, in *The Sea Surface and Global Change*, edited by P. Liss and R. Duce, pp. 121–172, Cambridge Univ. Press, New York.

Frew, N. M., and R. K. Nelson (1999), Spatial mapping of sea surface microlayer surfactant concentration and composition, in *Proceedings of the 1999 International Geoscience and Remote Sensing Symposium*, edited by T. I. Stein, pp. 1472–1474, IEEE Press, Piscataway, N. J.

Frew, N. M., J. C. Goldman, M. R. Dennett, and A. S. Johnson (1990), The impact of phytoplankton-generated surfactants on gas exchange at the air-sea interface, *J. Geophys. Res.*, *95*, 3337–3352.

Frew, N. M., E. J. Bock, W. R. McGillis, A. V. Karachintsev, T. Hara, T. Münsterer, and B. Jähne (1995), Variation of air-water gas transfer with wind stress and surface viscoelasticity, in *Air-Water Gas Transfer*, edited by B. Jähne and E. C. Monahan, pp. 529–541, AEON, Hanau, Germany.

Frew, N. M., R. K. Nelson, E. J. Bock, W. R. McGillis, J. B. Edson, and T. Hara (2002), Spatial variations in surface microlayer surfactants and their role in modulating air-sea exchange, in *Gas Transfer at Water Surfaces*, *Geophys. Monogr. Ser.*, vol. 127, edited by M. A. Donelan et al., pp. 153–159, AGU, Washington, D. C.

Garbe, C. S., B. Jähne, and H. Haußecker (2002), Measuring the sea surface heat flux and probability distribution of surface renewal events, in *Gas Transfer at Water Surfaces*, *Geophys. Monogr. Ser.*, vol. 127, edited by M. A. Donelan et al., pp. 109–114, AGU, Washington, D. C.

Gemmrich, J., and L. Hasse (1992), Small-scale surface streaming under natural conditions as effective in air-sea gas exchange, *Tellus, Ser. B*, *44*, 150–159.

Hara, T., E. J. Bock, and D. Lyzenga (1994), In situ measurements of capillary-gravity wave spectra using a scanning laser slope gauge and microwave radars, *J. Geophys. Res.*, *99*, 12,593–12,602.

Hara, T., E. J. Bock, N. M. Frew, and W. R. McGillis (1995), Relationship between air-sea gas transfer velocity and surface roughness, in *Air-Water Gas Transfer*, edited by B. Jähne and E. C. Monahan, pp. 611–616, AEON, Hanau, Germany.

Hara, T., E. J. Bock, J. B. Edson, and W. R. McGillis (1998), Observations of short wind waves in coastal waters, *J. Phys. Oceanogr.*, *28*, 1425–1438.

Haußecker, H. (1996), Measurements and simulation of small scale exchange processes at the ocean surface, Ph.D. thesis, 203 pp., Univ. of Heidelberg, Heidelberg, Germany.

Haußecker, H., U. Schimpf, C. S. Garbe, and B. Jähne (2002), Physics from IR image sequences: Quantitative analysis of transport models and parameters of air-sea gas transfer, in *Gas Transfer at Water Surfaces*, *Geophysical Monogr. Ser.*, vol. 127, edited by M. A. Donelan et al., pp. 103–108, AGU, Washington, D. C.

Higbie, R. (1935), The rate of absorption of a pure gas into a still liquid during short periods of exposure, *Trans. Am. Inst. Chem. Eng.*, *31*, 365–389.

Ho, D. T., W. E. Asher, L. F. Bliven, P. Schlosser, and E. L. Gordan (2000), On mechanisms of rain-induced air-water gas exchange, *J. Geophys. Res.*, *105*, 24,045–24,057.

Hühnerfuß, H., W. Alpers, W. D. Garrett, P. A. Lange, and S. Stolte (1977), Attenuation of capillary and gravity waves at sea by monomolecular organic surface films, *J. Geophys. Res.*, *88*, 9809–9816.

Hunter, K. A., and P. S. Liss (1980), Polarographic measurement of surface-active material in natural waters, *Water Res.*, *15*, 203–215.

Jähne, B. (1985), Transfer processes across the free water surface, Ph.D. thesis, Univ. of Heidelberg, Heidelberg, Germany.

Jähne, B., and H. Haußecker (1998), Air-water gas exchange, *Annu. Rev. Fluid Mech.*, *30*, 443–468.

Jähne, B., K. O. Münnich, and U. Siegenthaler (1979), Measurements of gas exchange and momentum transfer in a circular wind-water tunnel, *Tellus*, *31*, 321–329.

Jähne, B., W. Huber, A. Dutzi, T. Wais, and J. Ilmberger (1984), Wind/wave-tunnel experiment on the Schmidt number and wave field dependence of air/water gas exchange, in *Gas Transfer at Water Surfaces*, edited by W. Brutsaert and G. H. Jirka, pp. 303–309, D. Reidel, Norwell, Mass.

Jähne, B., K. O. Münnich, R. Bösinger, A. Dutzi, W. Huber, and P. Libner (1987a), On the parameters influencing air-water gas exchange, *J. Geophys. Res.*, *92*, 1937–1949.

Jähne, B., G. Heinz, and W. Dietrich (1987b), Measurement of the diffusion coefficients of sparingly soluble gases in water, *J. Geophys. Res.*, *92*, 10,767–10,776.

Jähne, B., P. Libner, R. Fischer, T. Billen, and E. J. Plate (1989), Investigating the transfer processes across the free aqueous boundary layer by the controlled flux method, *Tellus*, *Ser. B*, *41*, 177–195.

Jessup, A. T., C. J. Zappa, and H. Yeh (1997), Defining and quantifying microscale wave breaking with infrared imagery, *J. Geophys. Res.*, *102*, 23,145–23,153.

Ledwell, J. R. (1984), The variation of the gas transfer coefficient with molecular diffusivity, in *Gas Transfer at Water Surfaces*, edited by W. Brutsaert and G. H. Jirka, pp. 293–302, D. Reidel, Norwell, Mass.

Lee, Y. H., G. T. Tsao, and P. C. Wankat (1980), Hydrodynamic effect of surfactants on gas-liquid oxygen transfer, *AIChE J.*, *26*, 1008–1012.

Levich, V. G. (1962), *Physico-Chemical Hydrodynamics*, Prentice-Hall, Old Tappan, N. J.

Liss, P. S., and L. Merlivat (1986), Air-sea gas exchange rates: Introduction and synthesis, in *The Role of Air-Sea Exchange in Geochemical Cycling*, edited by P. Buat-Menard, pp. 113–127, D. Reidel, Norwell, Mass.

Lucassen-Reynders, E. H. (1986), Dynamic properties of film-covered surfaces, in *Role of Surfactant Films on the Interfacial Properties of the Sea-Surface*, edited by F. Herr and J. Williams, pp. 175–186, Off. of Nav. Res., London.

Lucassen-Reynders, E. H., and J. Lucassen (1969), Properties of capillary waves, *Adv. Colloid Interface Sci.*, *2*, 347–395.

McGillis, W. R., J. B. Edson, J. E. Hare, and C. W. Fairall (2001a), Direct covariance of air-sea CO_2 fluxes, *J. Geophys. Res.*, *106*, 16,729–16,745.

McGillis, W. R., J. B. Edson, J. D. Ware, J. W. H. Dacey, J. E. Hare, C. W. Fairall, and R. Wanninkhof (2001b), Carbon dioxide flux techniques performed during GasEx-98, *Mar. Chem.*, *75*, 267–280.

Melville, W. K., R. Shear, and F. Veron (1998), Laboratory measurements of the generation and evolution of Langmuir circulations, *J. Fluid Mech.*, *364*, 31–58.

Münnich, K. O., and D. Flothmann (1975), Gas exchange in relation to other air-sea interaction phenomena, paper presented at SCOR Workshop on Air-Sea Interaction Phenomena, Miami, Fla.

Münsterer, T., and B. Jähne (1998), LIF measurements of concentration profiles in the aqueous mass boundary layer, *Exp. Fluids*, *25*, 190–196.

Nightingale, P. D., G. Malin, C. S. Law, A. J. Watson, P. S. Liss, M. I. Liddicoat, J. Boutin, and R. C. Upstill-Goddard (2000a), In situ evaluation of air-sea gas exchange parameterizations using novel conservative and volatile tracers, *Global Biogeochem. Cycles*, *14*, 373–387.

Nightingale, P. D., P. S. Liss, and P. Schlosser (2000b), Measurements of air-sea gas transfer during an open ocean algal bloom, *Geophys. Res. Lett.*, *27*, 2117–2120.

Nilsson, C. S., and P. C. Tildesley (1995), Imaging of oceanic features by ERS-1 synthetic aperture radar, *J. Geophys. Res.*, *100*, 953–967.

Peltzer, E. T., and P. G. Brewer (1993), Some practical aspects of measuring DOC-sampling artifacts and analytical problems with marine samples, *Mar. Chem.*, *41*, 243–252.

Peng, T.-H., W. S. Broecker, G. G. Mathieu, Y. H. Li, and A. E. Bainbridge (1979), Radon evasion rates in the Atlantic and Pacific Oceans as determined during the GEOSECS program, *J. Geophys. Res.*, *84*, 2471–2486.

Romano, J.-C. (1996), Surface slick occurrence in the open sea (Mediterranean, Red Sea, Indian Ocean) in relation to wind speed, *Deep Sea Res.*, *Part I*, *43*, 411–423.

Schimpf, U., B. Jähne, and H. Haußecker (2002), On the investigation of statistical properties of the micro turbulence at the ocean surface, in *Gas Transfer at Water Surfaces*, *Geophys. Monogr. Ser.*, vol. 127, edited by M. A. Donelan et al., pp. 51–57, AGU, Washington, D. C.

Schimpf, U., C. Garbe, and B. Jähne (2004), Investigation of transport processes across the sea-surface microlayer by infrared imagery, *J. Geophys. Res.*, *109*, C08S13, doi:10.1029/2003JC001803, in press.

Scott, J. C. (1972), The influence of surface-active contamination on the initiation of wind waves, *J. Fluid Mech.*, *56*, 591–606.

Scott, J. C. (1975), The preparation of water for surface-clean fluid mechanics, *J. Fluid Mech.*, *69*, 339–351.

Siddiqui, M. H. K., M. R. Loewen, C. Richardson, W. E. Asher, and A. T. Jessup (2001), Simultaneous particle image velocimetry and infrared imagery of microscale breaking waves, *Phys. Fluids*, *13*, 1891–1903.

Siddiqui, M. H. K., M. R. Loewen, W. E. Asher, and A. T. Jessup (2004), Coherent structures beneath wind waves and their influence on air-water gas transfer, *J. Geophys. Res.*, *109*, C03024, doi:10.1029/2002JC001559.

Springer, T. G., and R. L. Pigford (1970), Influence of surface turbulence and surfactants on gas transport through liquid interfaces, *Ind. Eng. Chem. Fundam.*, *9*, 458–465.

Stewart, R. H. (1985), *Methods of Satellite Oceanography*, 360 pp., Univ. of Calif. Press, Berkeley.

Tans, P. P., I. Y. Fung, and T. Takahashi (1990), Observational constraints on the global atmospheric CO_2 budget, *Science*, *247*, 1431–1438.

Terray, E. A., M. A. Donelan, Y. C. Agrawal, W. M. Drennan, K. K. Kahma, A. J. Williams III, P. A. Hwang, and S. A. Kitaigorodskii (1996), Estimates of kinetic energy dissipation under breaking waves, *J. Phys. Oceanogr.*, *26*, 792–807.

Upstill-Goddard, R. C., A. J. Watson, J. Wood, and M. I. Liddicoat (1991), Sulfur hexafluoride and He-3 as seawater tracers—Deployment techniques and continuous underway analysis for sulfur hexafluoride, *Anal. Chim. Acta*, *249*, 555–562.

Veron, F., and W. K. Melville (2001), Experiments on the stability and transition of wind-driven water surfaces, *J. Fluid Mech.*, *446*, 25–65.

Vodacek, A., N. V. Blough, M. D. DeGrandpre, E. T. Peltzer, and R. K. Nelson (1997), Seasonal variation of CDOM and DOC in the Middle Atlantic Bight: Terrestrial inputs and photooxidation, *Limnol. Oceanogr.*, *42*, 674–686.

Wanninkhof, R. (1992), Relationship between wind speed and gas exchange over the ocean, *J. Geophys. Res.*, *98*, 7373–7382.

Wanninkhof, R., and W. R. McGillis (1999), A cubic relationship between gas transfer and wind speed, *Geophys. Res. Lett.*, *26*, 1889–1893.

Wanninkhof, R., W. Asher, R. Weppernig, H. Chen, P. Schlosser, C. Langdon, and R. Sambrotto (1993), Gas transfer experiment on Georges Bank using two volatile deliberate tracers, *J. Geophys. Res.*, *98*, 20,237–20,248.

Zappa, C. J. (1999), Microscale wave breaking and its effect on air-water gas transfer using infrared imagery, Ph.D. thesis, Appl. Phys. Lab., Univ. of Washington, Seattle.

Zappa, C. J., W. E. Asher, and A. T. Jessup (2001), Microscale breaking and air-water gas transfer, *J. Geophys. Res.*, *106*, 9385–9391.

Zappa, C. J., W. E. Asher, A. T. Jessup, J. Klinke, and S. R. Long (2002), Effect of microscale wave breaking on air-water gas transfer, in *Gas Transfer at Water Surfaces*, *Geophys. Monogr. Ser.*, vol. 127, edited by M. A. Donelan et al., pp. 23–29, AGU, Washington, D. C.

J. B. Edson, N. M. Frew, S. P. McKenna, and R. K. Nelson, Woods Hole Oceanographic Institution, Woods Hole, MA 02543, USA. (jedson@whoi.edu; nfrew@whoi.edu; sean.mckenna@ngc.com; rnelson@whoi.edu)

T. Hara, Graduate School of Oceanography, University of Rhode Island, Narragansett, RI 02882, USA. (thara@uri.edu)

H. Haußecker, Intel Corporation, Santa Clara, CA 95052, USA. (horst.haussecker@intel.com)

B. Jähne and U. Schimpf, Interdisciplinary Center for Scientific Computing, University of Heidelberg, 69120 Heidelberg, Germany. (bernd.jaehne@iwr.uni-heidelberg.de; uwe.schimpf@iwr.uni-heidelberg.de)

W. R. McGillis, Lamont-Doherty Observatory, Columbia University, Palisades, NY 10964, USA. (mcgillis@ldeo.columbia.edu)

B. M. Uz, Earth System Science Interdisciplinary Center, University of Maryland, College Park, MD 20742, USA. (uz@essic.umd.edu)